ELSEVIER

ADVANCES IN COLLOID AND INTERFACE SCIENCE

Advances in Colloid and Interface Science
82 (1999) 127–187

www.elsevier.nl/locate/cis

Foam in porous media: thermodynamic and hydrodynamic peculiarities

Konstantin G. Kornev[a], Alexander V. Neimark[b,*], Aleksey N. Rozhkov[a]

[a] *Institute for Problems in Mechanics, Russian Academy of Sciences, Prospect Vernadskogo 101, Moscow 117526, Russia*
[b] *TRI / Princeton, 601 Prospect Ave., Princeton, NJ 08542-0625, USA*

Abstract

Thermodynamic and hydrodynamic properties of foams in porous media are examined from a unified point of view. We show that interactions between foam films (lamellae) and wetting films covering the pore walls play an important role in treating experimental data and constructing a general theory of foam residence and motion through porous media. Mechanisms of in situ bubble generation, foam patterning, and rheological peculiarities of foams in pores are discussed in detail. In particular, we clarify the difference between foam lamellae and liquid lenses, focusing on intermolecular forces in thin foam and wetting films. A consistent description of conditions of mechanical equilibrium of curved lamellae, including dynamic effects, is presented for the first time. This microlevel approach enables us to describe the dependence of the capillary pressure in the Plateau border on the current state of the pair 'wetting film–foam lamella'. We review a theory of foam patterning under a load. Two driving forces are invoked to explain specific interactions between the solid skeleton and foams. The binding forces caused by bubble compressibility and the pinning forces due to capillarity determine a specific ordering of lamellae in porous media. The microscopic bubble train model predicts asymptotic expressions for the start-up-yield pressure drop. We consider key problems that underlay the understanding of physical mechanisms of anomalous foam resistance. Different micromechanical models of foam friction are

* Corresponding author. Tel.: +1-609-430-4818; fax: +1-609-683-7149; e-mail: aneimark@triprinceton.org

PII: S0001-8686(99)00013-5

thoroughly discussed. Bretherton's (1961) theory of the forced, steady fluid–fluid displacement is reviewed in application to bubble transport through pore channels. The origins of disagreement of the theory and experiment are discussed. The Bretherton theory is augmented based on a new sailboat model, which accounts for thermodynamic coupling of foam lamellae and wetting films. Special attention is paid to studies of stick-slip motion of lamellae and bubbles in pores of varying diameter. Finally, we discuss macroscale models and analyze topical problems of foam behavior in porous media, including reservoirs, granular, and fibrous materials.

Keywords: Foam; Lamella; Wetting films; Porous media; Foam patterning and flow

Contents

1. Introduction

Foams display a variety of behaviors that distinguish them into the special subject of interface science. The cell structure of foams, exhibiting foam irregularity, instability, chaos and the like, can be observed daily. The specific properties of foams have attracted the attention of researches for centuries. At the present time, a substantial collection of books and reviews [1–12], cover a wide range of fundamental questions. Especially when confined in porous media, foams have a unique hierarchical structure and rheological properties. Novel applications of foams in porous media have become an intriguing subject of fundamental, systematic studies. In particular, because of their extremely efficient blocking action, foams assist groundwater/soil remediation, selective blockage and extraction of oil or other liquids from porous materials. Industrial foam technologies include dyeing and finishing of textile fabrics, paper coating, resin-impregnation of fibrous mats and fabrics. However, while technologically effective, foams in porous media remain enigmatic. In this review, we discuss selected problems associated with the thermodynamics and hydrodynamics of foams in porous media. Earlier reviews [13–17] are useful guides to this branch of studies. We focus on the physical mechanisms governing foam flow and residence in confined geometries. Mechanistic models of foam evolution in bulk and in porous media, which are based on the population balance method [18,19], dynamic scaling [20–22], and also percolation models of foam flow in pore networks (see the latest review of Rossen [17] and references therein) are beyond the scope of this survey.

2. Thermodynamic peculiarities of foam distribution in confining systems

2.1. Bulk foam and foam films: capillary and disjoining pressures

Prior to analyzing the specifics of foam behavior in porous media, let us briefly review the properties of bulk foam. Bulk foam is often encountered in everyday life (soap foam) and nature (sea froth), and finds numerous technological applications including: fire fighting, surface and in situ cleaning, separations, etc. Traditional and potential applications of foam in engineering processes are reviewed by several authors [3,8,9,11].

Bulk foams are dispersions of gas bubbles in a liquid matrix. We distinguish between two types of foams. The first is the so-called quasi-spherical foam, a system of nearly spherical bubbles dispersed in a continuos liquid phase. This foam is similar to an emulsion. The second type, the focus of this review, is the so-called polyhedral foam, a system of coarsened bubbles separated by thin liquid films, usually called lamellae. The bubbles in polyhedral foams have a distorted polyhedral shape and may differ in their size and number of neighbors, which equals the number of polyhedral faces formed by the lamellae. The lamellae separating non-equal bubbles may be curved due to pressure differences between the bubbles.

Real foams are unstable, and evolve because a decrease in the lamella area leads

to a decrease in the interfacial free energy. The physical factors controlling foam evolution, patterning and stability are gravity-driven liquid drainage, interbubble gas diffusion caused by the pressure difference across the lamellae, and lamella thinning and rupture. To guarantee a long lifetime, the lamellae are stabilized by surface active molecules or surfactants, such as sodium lauryl sulfate and the like (which reduce the interfacial tension and establish an additional repulsion between the lamella surfaces), and additives, e.g. hydroxylethylcellulose, to increase the liquid viscosity.

Even in the ideal situation of an initially perfectly ordered foam, comprised of uniform bubbles with a uniform gas pressure, finite-size perturbations in bubble shape would lead to an irreversible growth of the larger bubbles at the expense of the smaller. This effect, known as coarsening [3] is unavoidable, yet can be slowed by using surfactants and additives. Although foam, as a non-equilibrium thermodynamic system, evolves in time, the instantaneous foam configuration may be regarded as a quasi-equilibrium configuration for the current distribution of pressures. The characteristic time to establish a local mechanical equilibrium between the bubbles and the lamellae is much smaller than the characteristic time for pressure changes due to mass transfer. Thus, the current distribution of pressures in the bubbles determines foam geometry.

Although global foam structure is difficult to quantify, mechanical equilibrium necessarily minimizes the surface free energy with respect to infinitesimal changes in the local configuration of bubbles and lamellae, determining the local geometry, or microgeometry of foams. Foam microgeometry was studied in detail by Josef-Antoine-Ferdinand Plateau over the course of a quarter century (1843–1869); for a contemporary description see Nitsohe [23].

The Plateau law, one of the most elegant physical laws of nature, can be formulated as follows: in 'dry' foams with a small liquid content, the lamellae between the bubbles form a polyhedral cell structure with certain universal features. The faces (lamellae) always meet three at a time at equal angles of 120° and form the edges named Plateau borders. The edges (Plateau borders) always meet each other in groups of four at the equal tetrahedral or Maraldi angle of $109°28''16'$, whose cosine equals $-1/3$. The four-way junctions of Plateau borders are usually referred to as vertices. The Plateau borders constitute a network of channels for liquid transport through the foam. The vertices can be regarded as the nodes of this network, and the Plateau borders as the bonds. These specific features of the foam microgeometry determine to a great extent the rheological, mechanical and transport properties of foams.

The Plateau law expresses the general condition of mechanical stability, provided that the lamellae are considered as hypothetical membranes with an inherent uniform surface tension. The validity of the Plateau law has been confirmed for various cellular systems including foams, biological tissues, polycrystals, and magnetic domains [6,10,23–26]. The Plateau law is not limited to cells with flat interfaces. but is valid for any foam, with curved lamellae between bubbles of different pressure. For curved interfaces, the inclination angles are measured between the planes tangent to the lamellae. Bolton and Weaire [27,28] have proven

the so-called decoration lemma and have shown that the Plateau law should be valid even in the case of thick Plateau borders, provided that the angles are measured using the perpendicular cross-section of the Plateau border between the extensions of the curved lamellae meeting in the center of the border.

In reality, the films between the bubbles tend to squeeze out liquid. Consider a single Plateau border in ideal uniform foam, assuming that all the lamellae are flat (Fig. 1). The curvature of the Plateau border walls causes a pressure difference across the walls, equal to the Laplacian capillary pressure,

$$P_c = P_g - P_w = \sigma\left(\frac{1}{r_1} + \frac{1}{r_2}\right), \tag{1}$$

where σ is the surface tension, r_i are the principal radii of curvature of a meniscus, P_g is the gas pressure and P_w is the hydrostatic pressure in the liquid. By virtue of the Laplacian capillary pressure P_c, the hydrostatic pressure within the edge will be reduced with respect to the gas pressure. On the other hand, we would expect that the hydrostatic pressure within the flat lamellae would be equal to the gas pressure. At first sight, even in perfectly ordered foam with uniform gas pressure, a pressure difference exists between the Plateau borders and the lamellae, and the liquid should be squeezed out of the lamellae into the Plateau borders. However, in stabilized foams, the local mechanical equilibrium in the liquid phase is ensured by the additional, disjoining, pressure acting in the lamellae, which counterbalances the difference between the gas and hydrostatic pressures. The disjoining pressure, introduced by Derjaguin [29], plays a key role in thin film stability.

Here, it should be remembered that the foam cannot be formed from an ordinary pure liquid, i.e. without a so-called foaming agent. The 'mother fluid' for foams, bubbles and lamellae under consideration, is practically restricted to surfac-

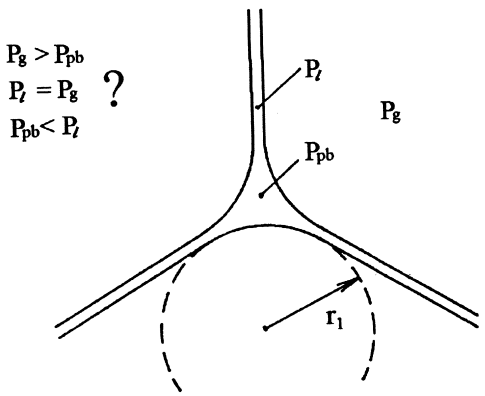

Fig. 1. Section through the Plateau border. P_l, pressure in lamellae; P_g, gas pressure; P_{pb}, pressure in the Plateau border.

tant solutions. Typically, the surfactant molecules have two dissimilar parts — one hydrophilic, tending to be surrounded by water; the other, hydrophobic, tending to be oozed out by the attractive forces between the water molecules. The surface active molecules concentrate at the lamella surfaces so that their hydrophilic heads are in water, while their hydrophobic tails reside outside (Fig. 2).

Drainage should occur until the lamella outer surfaces begin to 'feel' one another. For ionic surfactants, the electrostatic repulsion between the lamella surfaces prevents lamella bursting. Some other additives, either non-ionic or ionic (organic compounds, polymers, proteins, etc.), can also protect lamellae against bursting. The chemical and physical mechanisms of lamella stabilization have been intensively discussed [11,12,30–34]. The concept of disjoining pressure, which effectively accounts for the interactions between the lamella surfaces, allows us to quantitatively formulate the conditions of film equilibrium. Thermodynamic and experimental foundations of the existence of disjoining pressure in thin films were established almost 60 years ago in the pioneering papers of Derjaguin and Kussakov [35] and Derjaguin [36].

Disjoining pressure can stabilize perfectly ordered foam against small perturbations. Indeed, in thermodynamic equilibrium, the hydrostatic pressure within the lamellae equals that in the Plateau borders. Therefore, the capillary pressure is counterbalanced by the disjoining pressure, $\Pi(h)$, which is a function of the lamellae thickness, h:

$$P_c = \Pi(h). \tag{2}$$

Disjoining pressure can be either positive (disjoining) or negative (conjoining). The magnitude and the sign of this excess pressure depends upon the physico–chemical properties of the film and its environment. In particular, in wetting films, the disjoining pressure is affected by the properties of both pairs: the 'surrounding fluid-film' and the 'film-substrate'. The three characteristic types of disjoining pressure isotherms (Fig. 3) correspond to stable (1), metastable (2), and unstable (3) films. The second type, with two descending branches, is also common for foam films (Fig. 4). The first descending branch of the disjoining pressure isotherm corresponds to the Newton black films of the smallest thickness. The

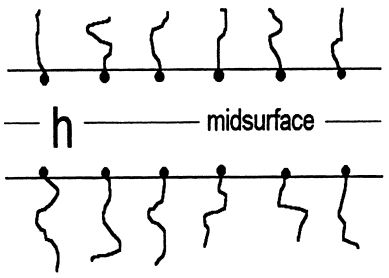

Fig. 2. Schematic illustration of the surfactant distribution over the lamellar surfaces.

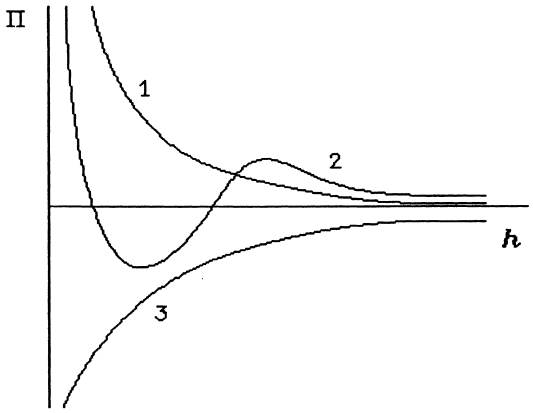

Fig. 3. A schematic illustration of typical disjoining pressure isotherms: (1) stable films; (2) metastable films; (3) unstable films (arbitrary units).

second descending branch corresponds to common black films [3,8,9,30]. The disjoining pressure isotherms vary with the type and concentration of the surfactant and electrolyte, or other foaming agents. The disjoining pressure isotherm of foam films intersects the h-axis when the film thickness exceeds a certain critical value (Fig. 4), i.e. equilibrium lamellae exist only within a narrow range of the film thickness.

Above a critical capillary pressure, the lifetimes of the lamellae and corresponding bulk foam become exceedingly short. Kruglyakov and Exerowa [8,9] analyzed the lifetime of bulk foam and individual foam lamellae with respect to the difference between the gas and liquid-phase pressures, i.e. in comparison to the capillary pressure. For a wide spectrum of experimental data, the thermodynamic properties of individual lamellae influence the lifetime of bulk foam. (For foams in porous media, a similar analysis has been performed by Aronson et al. [40]). The capillary pressure should correlate with the disjoining pressure in the lamella. Capillary pressure forces the lamella surfaces to come closer to one another. More stable foam results from foaming agents, which are able to form the Newton black films. Table 1 shows experimental data by Khristov et al. [41], for single films and bulk foam made from 0.001 M sodium dodecyl sulfate with a sodium chloride additive. The critical micelle concentration of the solution corresponds to 0.18 M NaCl [32].

If the initial lamella is a thick film, liquid depletion increases the capillary suction pressure on the lamella. The film thins to a critical thickness near the primary maximum and spontaneously jumps to the Newton film (Fig. 4). For sufficiently high capillary suction pressure, even along the stable branches of $\Pi(h)$, macroscopic disturbances may initiate rupture. Despite the long history of the transition from common black films to Newton black films, a standard explanation is lacking [2–4,8,9,30].

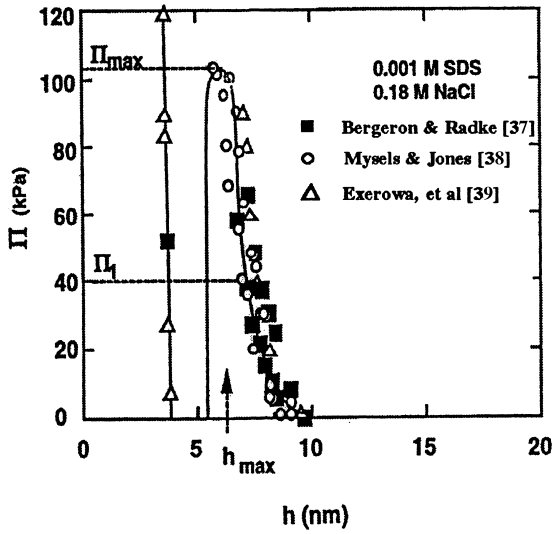

Fig. 4. Experimental disjoining pressure isotherm at room temperature for sodium dodecyl sulfate (SDS) in brine (NaCl) [37–39].

Thus, foam stability is highly sensitive to the thermodynamics of the lamellae, which also affects the topological structure of real foams. In particular, for Newton black films, the deviations of vertex angles from 120° can reach several degrees [42].

2.2. Foam patterning in porous media

Foam patterning in confining systems, such as porous media, has drawn attention only recently. Apparently, Fried [43] was the first to show that foam, because of its unique structure, reduces gas flow in porous media. Foam within porous media possesses a unique structure and rheological properties. In particular, in both pre- and in situ-generated foams, pore sizes impose constraints on the foam texture. If the characteristic bubble size is much smaller than the characteristic pore size, the

Table 1
Capillary pressures at which single films and bulk foams created from solutions of 0.001 M sodium dodecyl sulfate break [41]

NaCl concentration (mol l^{-1})	Film type	Critical capillary pressure (kPa)	
		Single film	Bulk foam
0.001	Ordinary thin	≥ 20	5
0.1	Common black	≥ 100	50
0.4	Newtonian black	≥ 120	100

foam confined in pores does not differ from bulk foam. In the opposite case, the foam in a porous medium is a network of thin liquid films (lamellae) spanning the pore channels.

The transition from the bulk phase to the 'pore-confined' regime is very complex and, as a rule, is discussed for ideal homogeneous capillaries or bead packs [44,45]. However, a more reasonable conceptual model of natural porous media is a network of interconnected capillaries of different sizes, which may contain constrictions and enlargements.

Recent experiments [46] show that the motion of pregenerated foam through channels with alternating narrow and wide regions demonstrates characteristic patterns. Just after the beginning of injection in a channel comprised of alternating narrow and wide parts, as depicted in Fig. 5, the lamella moves freely along the narrow part. If the wide part is free of foam, the lamella, reaching the junction, stops, blocked by the surface energy required to flow through the enlargement of the channel. The gas pressure stretches the lamella forming a bubble. The bubble either disappears, and the bubble swelling restarts when the next lamella reaches this point; or, after touching the wall of the enlargement, the lamella jumps to the free zone and stops in a new, downstream position. Advancing bubbles jump sequentially from the narrow to the wide parts of the channels and stop. When the wide part of the channel is filled entirely with foam, the first lamella passes freely through the next narrow part, and the process repeats in the next enlargement. The manner of foam generation makes the distance between the drifting lamellae of the same order as the length of the narrow regions. In doing so, the specific film channels of approximately the size of the narrow part of the original channel arise. In a quasi-steady state, when the channel is completely filled, the lamellae drift along the narrow zones freely while their flow through the effective channels in the enlargements looks like stick-slip motion. Therewith, advancing lamellae change

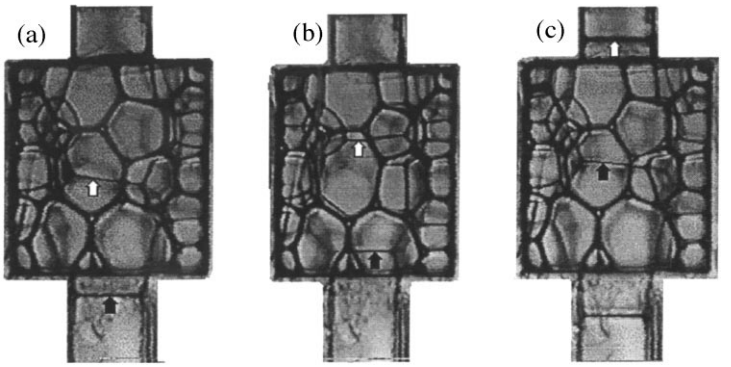

Fig. 5. The sequence of frames depicts the displacements of the lamellae in the enlargement of the channel [46]. Flow is from the bottom upwards. The white and black arrows indicate the positions of the pertinent lamellae at different times. The channel consisted of 10 cubic cell elements, 8 mm^3, and 10 narrow elements of 8-mm length, and 2.5 mm^2 cross-section.

the topology of bulk foam in the enlargements, and their motion is jumpy, due to the tendency of lamellae to minimize their surface energy. No rupture or birth of moving lamellae occur. When lamellae pass each other, the bulk foam in the enlargements deforms, but its structure does not change.

Foam flowing through the channel of an abruptly broadened cross-section, forms an effective channel, through which lamellae and gas are transported. The foam lamellae are astonishingly stable.

Such observations [46–48] favor a crucial role for the solid skeleton in foam patterning in porous media. In the presence of solid surfaces, the interface between the two fluids takes up configurations whose equilibrium and stability depend upon the contact areas and the interfacial free energies between the various phases. The solid skeleton imposes a structure, balancing the surface and capillary forces. The wetting films covering the pore walls compete with the lamellae. The energetics of lamellae and wetting films dominate foam behavior in porous media, especially in strong foams, with unbranched lamellae causing strong blocking of flows (see Fig. 6) [17,49,50].

2.3. Wetting films and menisci in pores: limiting capillary pressure

As an introduction to the distribution of phases in porous media, we briefly discuss an ideal capillary system of two immiscible fluids, gas and liquid, where the liquid wets the solid matrix completely, as for surfactant solutions and other liquids with a low surface tension.

In general, the solid matrix surface has a varying curvature, and (excluding external constraints such as gravity) if the pressure in the gas phase is constant, then, by the Laplacian capillary pressure acting on curved liquid–gas interfaces and the disjoining pressure acting in the wetting films, sets up a pressure gradient causing the liquid to flow. This flow tends to equalize the pressures and to establish constant curvature conditions over the menisci of the liquid–gas interface. The

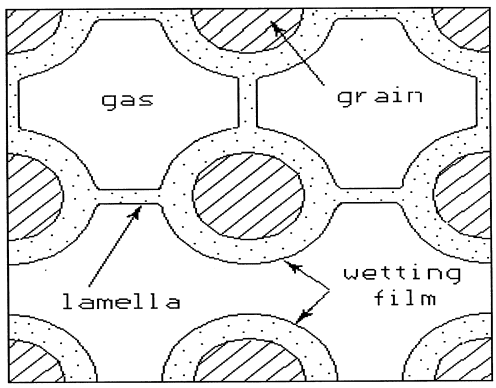

Fig. 6. Sketch of gas and liquid distribution in a strong foam in a granular medium.

wetting phase can form a bulk phase bounded by menisci and wetting films coating the varying curvature pore walls. The wetting films have a varying curvature and thickness to balance the capillary and disjoining pressures. How do the menisci coexist with the films?

A detailed thermodynamic theory of equilibrium between wetting films and menisci of the bulk fluid in pores of a different geometry [51–59], can be summarized as follows. In heterogeneous pore systems, the narrowest pore regions are completely filled with the wetting fluid held there by capillary forces. Thin films coat the walls of unfilled pores, interconnecting menisci of capillary held fluid. Consequently, fluid in pores is interlinked, and the local capillary and disjoining pressures are dependent throughout the entire global pore network due to this interlinking. Fluid flows rapidly in response to local changes in capillary pressure.

Drainage may cause thinning of wetting films and their transformations into ultra-thin films in the case of type 2 disjoining pressure isotherms (Fig. 3). In Fig. 3, the first stable branch of curve 2 (thinnest films), corresponds to so-called α-films of. thickness of a few molecular diameters, which behave as matrix-bonded films [54]. The second stable branch corresponds to the 'thick' β-films. A metastable β-film can undergo a spontaneous transition to a more stable state of α-film, sometimes, via 'rupture' of a thick β-film accompanied by the formation of a number of droplets, connected by α-films to the menisci in the pore corners [56,60] (Fig. 7).

As reported by Derjaguin and others, the probability of the formation of a critical nucleus of α-film depends upon the capillary pressure of the menisci, and upon the film surface area [56–58].

In foam coarsening, the transitions from metastable β-films to α-films are important also. Victorina et al. [61] and Churaev et al. [62] experimented with gas bubbles immersed in liquid-filled capillaries. A water-filled capillary with a gas bubble inside was placed in water-filled container with controlled external pressure. The bubble volume/length depends on the applied pressure in the liquid phase. When the liquid pressure was varied periodically, the authors observed hysteresis: after the first stage of the pressure decrease and corresponding bubble increasing in size, the initial bubble length could not be restored upon exceeding a certain critical length. The bubble extends irreversibly as the water pressure is

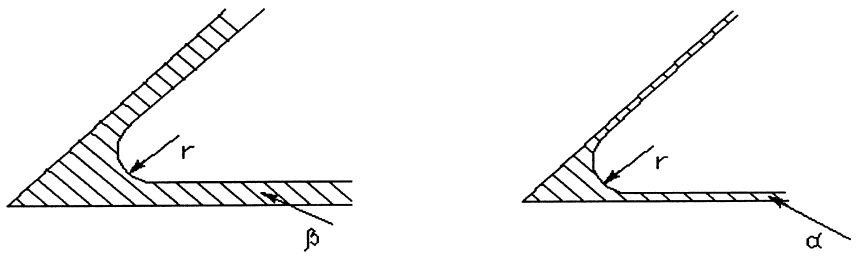

Fig. 7. Illustration of a transition from metastable β-films to α-films in a wedge [60].

decreased to a certain critical pressure drop. The menisci of such an extended bubble forms a finite contact angle despite their semi-spherical shape in the initial state. This effect has been explained by Derjaguin and co-authors as a transition of β-films, coating the capillary wall inside, into α-films

Thus, the transition of β-films to α-films can drastically change the global structure of the liquid-filled capillary network [63], and the conditions for generation, flow and residence of foam.

On the macroscale of a porous medium, the two-phase system is described by the capillary pressure or the Leverett function [54,64–66], which depends upon the saturation of one of the phases. This function links the pressures in coexisting phases and implicitly expresses the pressure difference, or the capillary pressure, via the local degree of saturation. In other words, the Leverett function serves as an equation of state for the two-phase system in the porous medium and determines foam patterning and rheology at a given degree of saturation. The 'macroscopic' capillary pressure reflects the main peculiarities of the pore network, with a critical capillary pressure above which no flux of the wetting fluid occurs in displacement experiments [64,65]. The associated saturation of the wetting phase is called residual saturation. In foams, however, the limiting capillary pressure also plays an important role [67].

The limiting capillary pressure is the pressure at which foam lamellae rapidly coalesce. Khatib et al. [67] experimentally studied the capillary pressure and the effluent bubble texture of foam generated before injection into sand or glass bead packs as the gas fractional flow is increased, while the gas flow rate stayed constant. Recall that the fraction of gas in the stream depends on the moving-gas saturation, estimated from the measured residence time of flowing gas [64,68]. The increase of gas fractional flow is associated with the growth of gas saturation, and correspondingly, with the increase in capillary suction. With increasing gas fractional flow at a constant gas flow rate, the capillary pressure approaches the limiting capillary pressure. At this pressure, foam coalescence causes the capillary pressure to drop abruptly and the foam texture to coarsen. So far, no model completely explains this phenomenon (reviewed in [17,50,69]). Foam demonstrates a characteristic of self-organized criticality [70–72]: coalescence and displacement of a coarse-textured foam usually maintains the capillary pressure near the limiting value [67,73].

2.4. Mechanisms of bubble generation in porous media: gas path closure

Foam may be forced (injected) into a porous medium, or it may be generated in situ. Garrett [34] has recently reviewed the injection of pregenerated foam into a porous medium. In-situ generated foams in the critical regime of limiting capillary pressure exhibit specific features. The three main mechanisms of in-situ foam generation are [48]: snap-off, lamella division and leave-behind (Fig. 8). Although all of these foam creation processes occur simultaneously, most authors believe that snap-off dominates blockage capability (e.g. [17,50]).

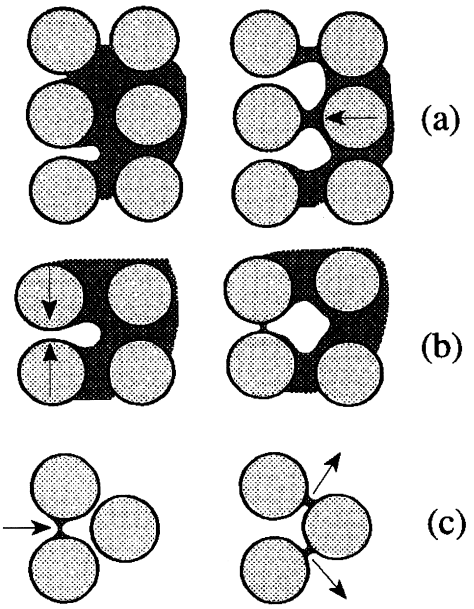

Fig. 8. Mechanisms of bubble generation in porous media. (a) 'Leave-behind': arrow indicates a lamella formed by gas fingering; (b) snap-off. when gas emerges from a wet constriction into a water-filled pore, the interface forces allow a leading portion of the gas to separate into a bubble; (c) lamellar division: arrows indicate the directions of movement [73].

Roof [74] proposed that bubbles or drops are generated on certain sites. Consider gas injection into a pore filled with a wetting liquid, with the pore modeled as the inside wall of a torus ('a bagel hole'), as analyzed by Mohanty [53]. This model reflects the main features of pore constrictions and allows some general conclusions about snap-off. We assume that the flow is slow enough to ensure that the liquid interfaces approximate their equilibrium shapes [53].

Three steps are key in bubble snap-off. First, the bubble moves into the constriction, depositing a film of wetting liquid (Fig. 9). We consider the wetting film as a layer of uniform thickness in the AT region. Then, the total curvature of the gas finger, $2H$, is approximately that of the pore wall in region AT, i.e.

$$2H(z) = -\frac{1}{r_m} + \frac{1}{R_H}. \tag{3}$$

In Figs. 9 and 10, r_t is the pore radius at the narrowest position (pore throat), point T; z is the axial distance from midpoint of the throat, R_H and r_m are the principal radii of curvature of the pore wall (r_m is the meridional radius of the torus). In region BC, the meniscus looks like a spherical cap of radius r_h. its

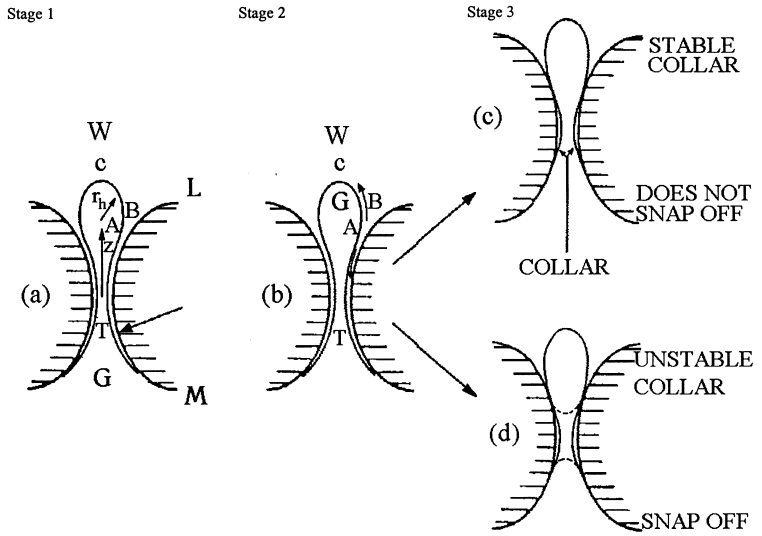

Fig. 9. Dynamics of collar formation in a toroidal pore. G, gas; W, water [53].

curvature becomes

$$2H_c = \frac{2}{r_h}. \tag{4}$$

The curvature must continuously vary from point A to point B. Therefore, the curvature of the gas–fluid interface has a minimum at point A. Whether the curvature in region BC is greater or less than that at point T depends on the extent of the gas protrusion, i.e. the value of radius r_b. The gas pressure is uniform, so, the pressure in the wetting phase P_w can be estimated using the Laplace equation of capillarity, Eq. (1), written in the form:

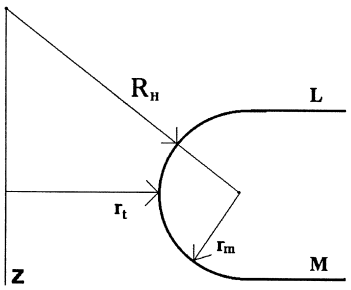

Fig. 10. Radii of curvature of the surface of revolution described by the curve LM in Fig. 9.

$$P_w = P_g - 2\sigma H, \tag{5}$$

Because the pressure P_w achieves a maximum at point A (Fig. 11), it drives the wetting fluid away from point A. Hence, the film pinches down at point A. At the same time, the wetting fluid, which resides between points A and B, will migrate toward the throat, point T, its interface taking the shape of a constant curvature surface. The accumulation of the wetting fluid at the throat is usually referred to as a *wetting collar* [48,53]. The flow rate limits the volume of the growing collar through hydraulic constraints. Therefore, we select as possible shapes the collar and the lens, which are stable to volume conserving perturbations. Fig. 12 demonstrates the characteristic features of the transition 'stable collar to stable lens' [75]. If the volume of the wetting film collected at the throat is small, it can be accommodated in a wetting collar around a stable neck meniscus, points A-B-C. But if the volume is larger than the maximum stable collar volume, point C, then the collar snaps off, creating a lens of wetting fluid at the throat.

The schematic illustrates that the hydrodynamics of gas fingering is a secondary factor in lens formation because capillary forces dominate. Hence, the problem of the bridging transition has, mainly, a thermodynamic, rather than as hydrodynamic, origin, resembling capillary condensation in pores [54,57,58]. Recall that if a solid surface is placed in contact with a vapor of wetting liquid, an adsorption film is formed. The film thickness depends on the vapor pressure and surface curvature. In narrow pores, as the vapor pressure increases, the films on the opposite walls of the pore coalesce and form a lens as the film thickness exceeds a specific value for a given pore geometry. Capillary condensation has been studied for different pore geometries. In particular, Everett and Haynes [76] comprehensively explained the example of a cylindrical capillary, spherical particles have been studied in detail by Neimark [77] and Neimark and Rabinovich [78,79]. Disjoining pressure effects have been included (e.g. [54,56]).

Turning to the problem of foam distribution, the most important conclusion is

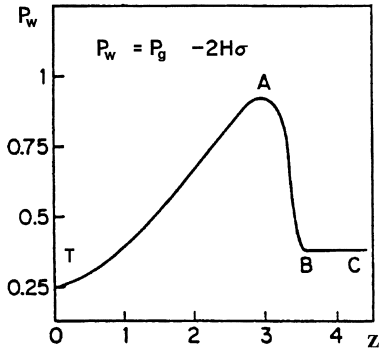

Fig. 11. The pressure (arbitrary units) in the wetting film at the end of the second stage [53].

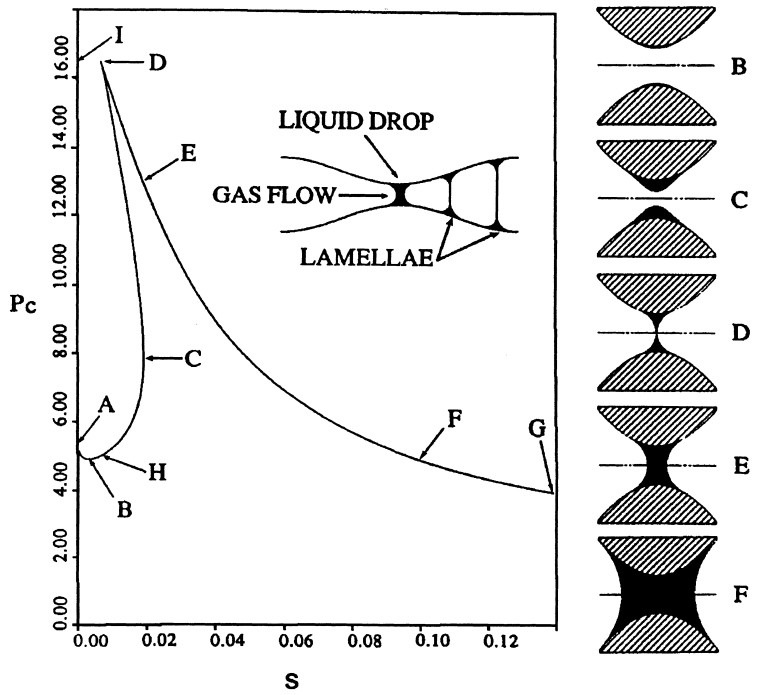

Fig. 12. The typical capillary pressure P_c (arbitrary units) as a function of the liquid saturation S (fraction of liquid phase within the pore, arbitrary normalization) for a pore shape which is a surface of revolution [75].

that the pore size, r, where foam lamellae may occur, can be estimated using the condition of thermodynamic stability for a film coating the pore walls.

For a cylindrical capillary, following Derjaguin's supposition of the additive action of the capillary and surface forces in curved wetting films, the capillary pressure in the bulk liquid, in equilibrium with the film in the cylindrical capillary, equals:

$$P_c(h) = \frac{\sigma}{r-h} + \Pi_w(h), \tag{6}$$

here Π_w is the disjoining pressure of the wetting film and r is the radius of the capillary. The film stability condition is defined by the inequality $\partial P_c/\partial h \leq 0$ [56], namely:

$$\frac{\sigma}{(r-h)^2} + \Pi'_w(h) \leq 0.$$

So the upper limit of thickness for a thermodynamically stable film, h_c, is defined

by,

$$\Pi'_w(h_c) = -\frac{\sigma}{(r - h_c)^2},$$

and the corresponding capillary pressure by Eq. (6) at $h = h_c$. Eq. (6) assumes that the disjoining pressure in the curved film can be approximated by the disjoining pressure isotherm for flat films, which is credible when $h \ll r$, and the radius of the capillary is greater than the characteristic length of action of molecular forces. The estimate is a required condition for lamellae to be generated by capillary instability.

A similar thermodynamic approach describes the process of bubble generation in mesoporous catalysts due to liquid decomposition [80]. However, in the nanometer scale pores fluid–solid interactions should be taken into account explicitly [81–85]. Modifying the conditions for capillary condensation, density functional theory gives a better understanding of capillary condensation phenomena in nanoconfinements (e.g. [86,87]).

Thus, whether or not the lens generation takes place at a potentially generating site depends on the capillary pressure, which is always limited from below. At least two pressures are related to snap-off phenomenon (dynamic capillary condensation): the pressure required for snap-off, P_{sn}, and the pressure P_{sh} required to displace wetting liquid from the pore throat. As a rule. $P_{sh} > P_{sn}$. Thus, for snap-off, the capillary pressure must first rise and then fall (Fig. 11). The ratio $P_{sn}/P_{sh} \approx O(1)$ is a function of the pore geometry and the substrate wettability [17,53,74], e.g. $P_{sn}/P_{sh} = 1/2$ for a wide cylindrical capillary [74].

2.5. Transformation of lens into lamella

When a surfactant is present, the configuration at point D (Fig. 12) with two interfaces touching one other, may be stable. A stable flat lamella may form as the result of the transition of the 'thick' film (with bulk solution properties) to a new thermodynamic state. The characteristic feature of such a transition is the appearance of a contact angle between the film and the bulk liquid [4,88,89].

Consider a simplified physical model of lamella formation from a lens spanning the cylindrical capillary of radius R (Fig. 13) [93]. This is the limiting case of the toroidal pore when $r_m \to \infty$ and $R = r_t = R_H$. Under the capillary suction pressure, which here equals $P_g - P_w = \rho_{\text{liquid}} gH$, the lens squeezes and forms a lamella of radius R_0 (see notes in Fig. 13). In sufficiently wide pores (10–100 μm wider), the characteristic size of the meniscus is greater than the characteristic size of transition zones between the thin liquid film and the bulk liquid [90–92]. Therefore, in the description of the transition from a lens to a lamella, classic thermodynamics, in which disjoining pressure effects are neglected, seems suitable. Then contact conditions may be modeled via the contact angles of the meniscus with the substrate, $\theta_{R,}$ and with the lamella, $2\theta_{0.}$

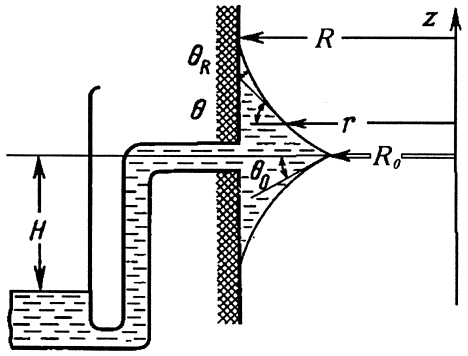

Fig. 13. Idealized picture of lamella formation within a tube [93].

The equilibrium shape of the meniscus can be obtained by integrating the Laplace equation

$$2H\sigma = \frac{1}{r}\frac{\mathrm{d}}{\mathrm{d}r}(r\sin\theta) = P_g - P_w = P_c, \qquad \tan\theta = \frac{\mathrm{d}z}{\mathrm{d}r}. \tag{7}$$

Eq. (7) has the integral

$$r\,\sin\theta = \frac{P_c}{2\sigma}r^2 + B,\ B = \text{const} \tag{8}$$

Making use of the boundary conditions $\mathrm{d}z/\mathrm{d}r = \tan\theta_0$, $r = R_0$, and $\mathrm{d}z/\mathrm{d}r = \tan\theta_R$, $r = R$ we find the relation between the capillary suction pressure and the lamella radius R_0 as:

$$\frac{RP_c}{2\sigma} = \frac{\cos\theta_R - \alpha\sin\theta_0}{1-\alpha^2}, \tag{9}$$

where $\alpha = R_0/R$. This equation demonstrates hysteresis in lamella formation. Indeed, as soon as the capillary suction pressure reaches a value $P_g - P_w = P_0 = 2\sigma\cos\theta_R/R$, the lens immediately generates a lamella of radius r_0^*. If the pressure rises, the lamella radius increases monotonically. If the capillary suction pressure decreases, the lamella shrinks to a critical radius $r_{0\min}$, then suddenly disappears. The critical radius $r_{0\min}$ minimizes Eq. (9).

Zorin et al. [93] performed a detailed experimental analysis of lamella formation by interferometry in transmitted light [94]. Water solutions of sodium dodecyl sulfate (SDS) and sodium chloride (NaCl) were used as liquids. The authors used capillaries of radius $R = 120$ μm drilled within a finegrained filter, $\theta_R \approx 0$. Fig. 14 demonstrates the characteristic features of the transition. Line 1 corresponds to a solution of 0.32 M (NaCl) + 0.05% (SDS), $\sigma = 31.8$ mN m^{-1}, and line II a solution

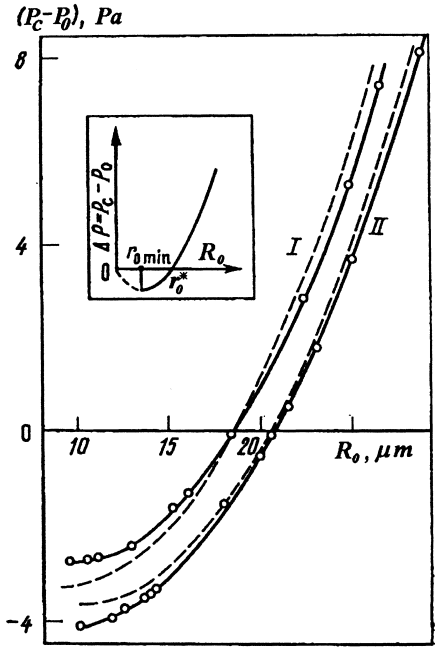

Fig. 14. The capillary pressure as a function of the lamella radius. Dashed lines represent the theoretical curves obtained by ignoring the action of the line tension [93].

of 0.45 M (NaCl) + 0.05% (SDS), $\sigma = 31.25$ mN m^{-1}. The contact angle θ_0 and the line tension κ of lamella were also measured. The latter is defined as

$$\gamma = 2\sigma\cos\theta_0 - \frac{\kappa}{R_0},$$

where γ is the lamella tension. For the first solution, the line tension was $k_I = 3 \times 10^{-9}N$, for the second $k_{II} = -1.5 \times 10^{-9}N$. For both solutions within the whole range of the measured lamella radii, the contact angle $2\theta_0$ was close to $\pi/10$.

In this model, the lamella contact angle $2\theta_0$ and the lamella tension are assumed to be constant. Thermodynamics of lamella tension and contact angle, which are indeed functions of lamella thickness and disjoining pressure, was elaborated by Kralchevsky et al. [95]. Because of the overlapping of the interfacial layers, in thin films like foam lamellae, the film tension becomes a function of the disjoining pressure and film thickness [4,57,58]. When the film thickness exceeds a few nanometers, the film tension γ usually differs only slightly from twice the value of the surface tension, σ, of the interface between the bulk solution from which the film is made and the surrounding phase [90]. Nevertheless, even this small deviation causes a finite contact angle between the meniscus and the lamella. We

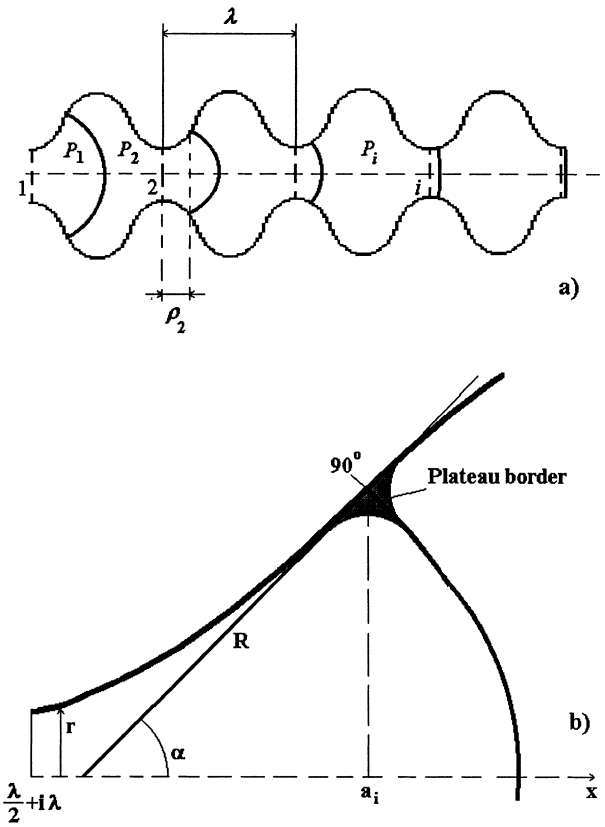

Fig. 15. (a) Scheme of lamellae distribution in a bamboo-like channel. Dashed lines are the initial positions of lamellae, and bold lines represent the lamellae under a load. (b) Parameters needed for calculation of the bubble volume variation and capillary force.

present the relation between the lamella tension and its disjoining pressure without proof (e.g. [4]):

$$\gamma = 2\sigma_f + \Pi(h_{ii+1})h_{ii+1} = 2\sigma + \int_{h_{ii+1}}^{\infty} \Pi(h)\mathrm{d}h + \Pi(h_{ii+1})h_{ii+1}. \tag{10}$$

Note, that his relation is valid for flat lamellae and may serve as a reasonable approximation for curved lamellae.

2.6. Lamellae in convergent (divergent) pores

The thermodynamic stability of curved lamellae, spanning convergent (divergent) pores, differ from those of flat lamellae. For simplicity, consider a pore channel as a cylindrical capillary with a radius that varies periodically with the distance (Fig. 15).

To study how the lamella thickness depends upon the pressure drop, acting across a curved lamella, one must generalize the Laplace formula for films with finite thickness. Using statistical average, Buff [96] showed how the Gibbs thermodynamic surface tension [97] can be determined (reviewed in [98–102]). A sophisticated thermodynamic analysis of curved thin films has been done by Ivanov and Kralchevsky [103]. We, however, use a somewhat simplified model of the thin film, in which the disjoining pressure acts as an additional load distributed over each lamella surface [35,36]). The model assumes that the contributions of capillary and surface forces are additive.

Thus, assuming that the inequality $P_i < P_{i+1}$, holds, the balance of forces at the interface from the side of i-th bubble gives the following expression [42,57,58]

$$P_i + \frac{2\sigma}{R_{ii+1}} = \Pi(h_{ii+1}) + P_w, \tag{11}$$

where h_{ii+1} is the film thickness, $\Pi(h)$ is the disjoining pressure isotherm of a flat lamella, R_{ii+1} is the mean radius of curvature of the lamella, provided that the film thickness is much less than the radius of curvature and σ is the surface tension of bulk liquid. Note that the use of the film surface tension, σ_f, defined for flat films through Eq. (10), in Eq. (11) instead of the bulk value, σ, leads to inconsistent corrections.

For the interface between the liquid film and bubble $i + 1$, the symmetric equation holds,

$$P_{i+1} - \frac{2\sigma}{R_{ii+1}} = \Pi(h_{ii+1}) + P_w. \tag{12}$$

Eqs. (11) and (12) imply that the ordinary Laplace equation for a thick film between two phases gives the mean radius of film curvature:

$$R_{ii+1}^{-1} = \frac{(P_{i+1} - P_i)}{4\sigma} \tag{13}$$

and the isotherm of the disjoining pressure gives the film thickness as:

$$\Pi(h_{ii+1}) = \tfrac{1}{2}(\Delta P_{i+1} + \Delta P_i), \tag{14}$$

where $\Delta P_i = P_i - P_w$, is the capillary overpressure in the i-th bubble.

First order corrections for a finite film thickness lead to the substitution of the bulk surface tension σ by the film tension γ as defined by Eq. (10). However, these corrections seem to be insignificant for practical estimates.

Recall that the capillary overpressures in Eq. (14) can be expressed via the disjoining pressure isotherms prescribed for 'substrate-wetting film-gas' conditions, i.e. via the background capillary pressure $P_c = P_i - P_w$. Thus, the equilibrium properties of curved lamellae also depend upon environmental conditions.

Eq. (13) has many solutions, i.e. lamellae might be placed at different positions

along the pore. However, the mechanical equilibrium conditions at the contact line impose a selection criterion for lamella positions within an axially symmetric pore. Discussing mechanical equilibrium, we can ignore the Plateau borders and assume that the lamella intersects the pore walls at a 90° angle, as observed experimentally [48].

Eq. (13) reflects minimization of film surface areas (see Fig. 15):

$$R_{ii+1} = r/\sin\alpha(r)\,|_{x=a_i}, \qquad \tan\alpha = \frac{\mathrm{d}r}{\mathrm{d}x}. \tag{15}$$

where x is the longitudinal coordinate, $r = r(x)$ is the pore profile, and a is the lamella chord coordinate. Laplace Eq. (13) defines the equilibrium locations of lamella for a given pressure differential; variations of the pressure differential lead to varying equilibrium lamella positions. However, not all the equilibrium configurations are stable. For stability, a small shift in the lamella position must give rise to a net restoring force, implying [104]

$$\frac{\mathrm{d}}{\mathrm{d}x}\left(P_{i+1} - P_i - \frac{4\sigma}{R_{ii+1}}\right) < 0. \tag{16}$$

If the pressure differential does not depend on the lamellar position, the stability condition depends only on the shape of the channel through Eqs. (15) and (16). Then Eq. (16) shows that stable equilibrium lamellae can exist only over convex, $\mathrm{d}\alpha/\mathrm{d}x < 0$, segments of the pore channel. If, however, the pore has both convergent and divergent parts, then the equilibrium positions correspond to all local extremum points of the channel radius. Minimum corresponds to stable and maximum to unstable equilibrium positions; because the larger the lamella perimeter is, the larger its surface energy.

2.7. Chain of lamellae: correlation length

Capillary forces tend to fix the lamellae at the pore throats, while elastic forces, caused by gas compressibility, shift the lamellae into new equilibrium positions, resulting in the equilibrium states observed in experiments. The situation resembles 'commensurate–incommensurate' phase transitions in solid state physics [105,106] and related problems, in which binding and pinning forces compete [107–112]).

Specific features can be revealed by the simple one-dimensional bubble train model [113–115]. Imagine a wavy channel as a rigid capillary with radius,

$$r = r_0 + \delta\cos\left(\frac{2\pi x}{\lambda}\right), \tag{17}$$

where the x-axis coincides with the capillary axis of symmetry. r_0, λ, and δ are characteristic scales of the porous medium. Assume, for simplicity, that the pore

aspect ratio is low, $(\delta/r_0 \ll 1$. This assumption, however, can be altered without changing most of the physical conclusions.

Consider the train of N lamellae, whose chord centers lie at $x = a_1,a_2,...,a_N$. and assume that in the initial undeformed state, the foam is perfectly ordered, with the lamellae connected by links (bubbles, or train carriages) of 'carriage length' $K\lambda$ with integer K.

Under a load, the i-th bubble is deformed, to a length $a_i - a_{i-1}$ with an accuracy of $O(\delta/r_0)$, [113–115]. The resulting elastic force acting upon the i-th lamella can be written with the same accuracy as:

$$f_e = \pi r_0^2 (P_{i+1} - P_i) \tag{18}$$

Making use of the ideal gas law, yields

$$P_{i+1}(a_{i+1} - a_i) = P_i(a_i - a_{i-1}) = \ \ldots = P_g K\lambda, \tag{19}$$

where P_g is the initial gas pressure in an individual bubble. We introduce a new function, ρ_i the displacement of the i-th lamella from its initial position at the throat. Then $a_i = iK\lambda + \rho_i + \lambda/2$ and Eq. (19) takes the form:

$$\rho_{i+1} - \rho_i = \frac{P_g K\lambda}{P_{i+1}} - \lambda K, \tag{20}$$

Note that the capillary force has a form similar to Eq. (18), but where the Laplacian pressure drops, Eq. (13) replaces the pressure differential. Then the balance of capillary and elastic forces gives, with accuracy $O(\delta/r_0)$, the equation

$$P_{i+1} - P_i = -\frac{8\pi\delta\sigma}{\lambda r_0}\sin\left(\frac{2\pi\rho_i}{\lambda}\right). \tag{21}$$

The boundary conditions for the 0th and the last, $N - 1$. lamellae are,

$$P_0 = P_g P_{\text{ext}}, \quad P_N = P_g P, \tag{22}$$

where P_{ext} and P are the dimensionless external pressures applied to the train. Thus all lamellae in the loaded train obey Eqs. (20)–(22). The corresponding Cauchy problem for the Ulam map [Eqs. (20) and (21)] in a different context [109], applies to foam patterning and to foam elasticity.

To estimate the limits of validity of the continuum mechanics, consider the linearized version of Eqs. (20)–(22), i.e. the asymptotic case of $\rho_i \to 0$, P, $P_{\text{ext}} \to 1$. For the semi-infinite train $N \to \infty$ the solution can be written in the form [116],

$$\rho_i = a\exp(-wi),$$

where a is a constant defined by the boundary conditions, and W satisfies the following transcendental equation:

$$\cosh\ w = 1 + 2\pi^2 K\mu \tag{23}$$

Here, the parameter

$$\mu = \frac{4\sigma\delta}{P_g r_0 \lambda}, \tag{24}$$

measures the strength of capillary forces with respect to elastic forces. In regimes where cooperative properties of foam play a crucial role, $K\mu \ll 1$, and the screening length (correlation length) $N_{\mathrm{cor}} \approx 1/w$ of a train is estimated as:

$$N_{\mathrm{cor}} \approx \frac{1}{2\pi\sqrt{K\mu}}, \quad K\mu \ll 1. \tag{25}$$

In the opposite case, when either gas compressibility or carriage length are large, pinning forces dominate binding ones, so:

$$N_{\mathrm{cor}} \approx \frac{1}{\ln(2 + 4\pi^2 K\mu)}, \quad K\mu \gg \frac{1}{4\pi^2}. \tag{26}$$

Explicit barrier $K\mu = 1/4\pi^2$ is the stability criterion for two bubbles [115]. Thus. in the former case, the load is distributed over a large number of lamellae. In the latter case, the first few lamellae bear most of the load. Therefore, the continuum model [Eqs. (20)–(22)] applies to foam patterning when $K\mu \ll 1$; and discrete effects should be taken into account for $K\mu \gg 1/4\pi^2$. The above mentioned inequality assigns a specific meaning to the terms of *compressible* and *incompressible* and determines the range of parameters over which a theory of foam elasticity can be constructed.

Restriction (25) allows simplified physical treatment [117]. Consider two characteristic values of pressure perturbation associated with foam in porous media on the microlevel of pores. The first characteristic pressure drop is the Laplacian capillary barrier $\delta P_c \approx 4\sigma/r_0$ imposed by the inherent structure of the pore matrix. This pressure drop is required to push a single lamella through a pore constriction. To estimate the second pressure variation caused by the change of bubble volume, we imagine displacing a single lamella, with other lamellae remaining at their initial positions. For an ideal gas, the pressure perturbation within the deformed bubble is $\delta P_g \approx P_g \delta V/V \approx P_g / K$, where V is the initial cell volume. This pressure variation does not depend on the external pressure drop, and is an inherent characteristic of the foam. We expect that whenever $P_g/\delta P_c > 1$ $(4\sigma K / P_g r_0 < 1)$, the foam will move as a whole, because the external pressure drop will be redistributed over all foam cells. In the opposite case, lamellae withstand variations of pressure of order P_g, so the ability of each lamella to sustain a local pressure variation of order P_g determines foam patterning.

2.8. Superstructures: analysis of the phase portrait

Phase portraits clarify the possible equilibrium states of trains with different interparticle interactions [106,111–115]. In the continuum limit, going over from a discrete variable to a continuous variable $s = 2\pi Ki$, and introducing dimensionless variables and functions $2\pi\rho_i/\lambda \to \rho$, $P_i/P_g \to \rho$, we rewrite Eqs. (20) and (21) as:

$$-\frac{dp}{ds} = \frac{\mu}{K}\sin\rho. \tag{27}$$

$$\frac{d\rho}{ds} = \frac{1}{p} - 1, \tag{28}$$

Eqs. (27) and (28) has first integral,

$$\ln p - p = E + \frac{\mu}{K}\cos\rho, \tag{29}$$

where E is a constant. The translational symmetry $\rho \to \rho + 2\pi n$, $n = 0, \pm\infty$, allows us to consider Eqs. (27) and (28) over the whole range, $\rho \in (-\infty,\infty)$. The phase portrait (Fig. 16) shows two kinds of singular points: hyperbolic and elliptic (see also [106]).

Points $p = 1$, $\rho = 2\pi n$, $n = 0 \pm \infty$ are hyperbolic, representing configurations of the bubble train where lamellae are attached to the narrowest parts of the channel; so that the surface energy of lamellae is minimal. Points $p = 1$, $\rho = \pi(2n + 1)$, $n = 0, \pm\infty$ are elliptic, with cycles describing states in which lamellae avoid wide parts of the channel because the surface energy is maximal. The hyperbolic points are connected by a separatrix, which has two branches within each period of the phase portrait. One exits the left point. passes above the line

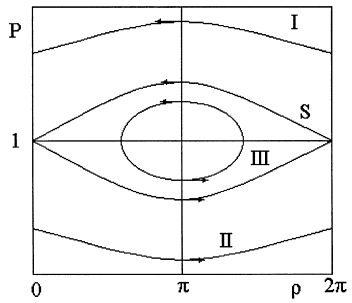

Fig. 16. Phase portrait of the system [Eqs. (27) and (28)]. The separatrix is denoted as 'S'. Arrows show the direction of the increasing arclength s.

$p = 1$ and enters the right hyperbolic point. The other branch goes in the opposite direction under the line $p = 1$. The separatrix is described by,

$$\ln\ p - p = \frac{\mu}{K}(\cos\rho - 1), \tag{30}$$

which follows from Eq. (29). At the separatrix,

$$E = E^{**}, \quad E^{**} = -1 - \frac{\mu}{K}. \tag{31}$$

The separatrix subdivides the phase plane (p, ρ) into three parts. Parts I and II represent infinite slippage $(E < E^{**})$, while part III corresponds to bounded motion $(E > E^{**})$. All integral curves in domain III pass through points at which $p_N = 1$, so they describe bubble trains with free boundary lamellae. The integral curves of domain I correspond to a bubble train with a blocking lamella at $\rho_{N-1} = 0,\ p_N > 1$. Domain II represents extended bubble trains with fixed boundary lamellae $\rho_{N-1} = 0,\ p_N < 1$ Each of the singular points $p = 1,\ \rho = 2\pi n,$ creates four branches of the separatrix corresponding to the configurations of the chain.

Therefore, if some pattern incorporates a single or a few singular points, the respective texture of the train will be complex. If we associate the current number of lamellae with time, then the finite motion in domain III can be treated as a motion with a finite period T, i.e. the number of bubbles accumulated by a single cycle is finite. Near the separatrix, T tends to infinity, i.e., the solution describes an unconfined bubble train. The solution also demonstrates the effect of the 'irreversibility' of bubble train displacement. After the action of a critical pressure drop some of the lamellae never recover their former positions (Fig. 17). The solution looks like a solitary 'domain wall' [106–111,113].

$$\rho = 4\tan^{-1}\exp - [(x - x_0)] + O\left(\sqrt{\frac{\mu}{K}}\right), \quad x = \sqrt{\frac{\mu}{K}}s. \tag{32}$$

For a given pressure drop, all the lamellae behind the 'wall' at $s \to -\infty$ shift by the period $\rho = 2\pi$ and stay there after unloading. Lamellae at $s \to \infty$, ahead of the wall, keep their undeformed state $\rho = 0$. The domain wall matches the second zone (the undisturbed zone) where the lamellae are pinned at the equilibrium state with the first zone, where lamellae are displaced by one period (Fig. 17). The wall thickness can be estimated as $O(\lambda\sqrt{K}/\sqrt{\mu})$ [113].

The continuous model [Eqs. (27) and (28)], is valid whenever collective effects dominate and lamellar displacements and pressure vary weakly over the train. In the opposite case, the discrete map [Eqs. (20) and (21)] resembling the Ularn model [112,118]) has stochastic solutions [114,115]. Discreteness results in more complex foam patterning; in particular, glass-like ordering of lamellae. The ability of

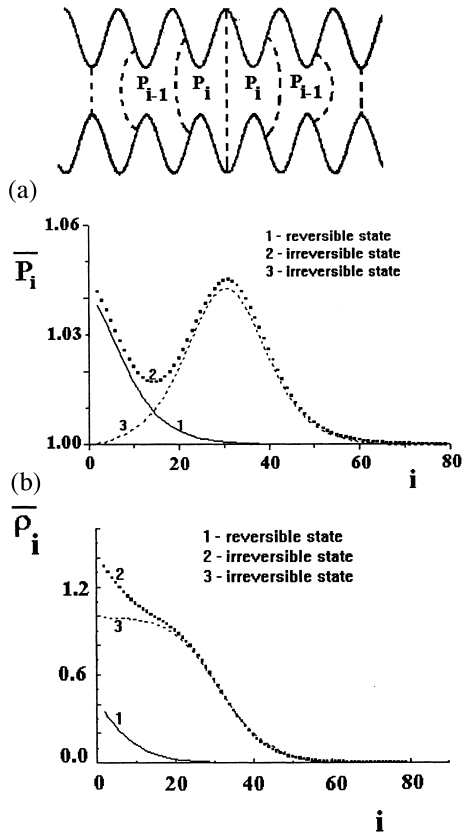

Fig. 17. (a) Sketch of a domain wall and the pressure distribution $\overline{P}_i = P_i/P_g$ over the chain; 1, 2 — chain under load; 3 — after unloading. (b) The displacements of lamellae $\overline{\rho}_i = \rho_i/\lambda$; 1, 2 — chain under load; 3 — after unloading. $N = 80$, $\mu = 10^{-3}$, $K = 1$.

variations of the initial data ρ_{N-1} to abruptly alter the chosen branch of the separatrix and the sensitivity to the initial data of the distribution of the points along the trajectory manifest through chaotic ordering. While the domains may occupy varying regions, the associated energy remains almost the same [114,115].

Sensitivity to initial conditions results from the finite correlation length. Fig. 18 shows the phase portrait associated with glass-like patterning.

2.9. Start-up pressure drop

The previous analysis shows that, in porous media, foam drastically changes the rheological behavior of the gas phase. In a foam, gas flows as if it were an homogeneous fluid, with a start-up yield pressure drop, required to initiate flow through porous media [14,17,45,50,119].

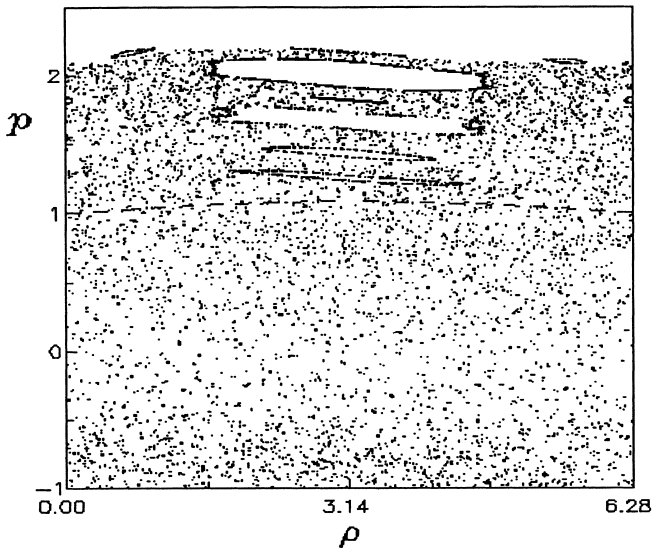

Fig. 18. The typical phase portrait for Eqs. (20)–(22), $\mu = 0.016$, $K = 10$, $N = 2000$, and six starting points. The dashed line represents the separatrix of the continuous model [114,115].

The explanation of the yield pressure drop usually assumes that foam is incompressible [120], leading to an enormous capillary barrier. Considering capillarity solely, we estimate the pressure required to displace a lamella from the pore as approximately $\Delta P_{\text{ind}} \approx 4\sigma/r_0$. We can also estimate a similar barrier for a strong foam, assuming that before deformation foam lamellae are attached to each throat so that the distance between them is of the order of the pore radius, $r \approx r_0$. If we neglect the gas compressibility, we need to overcome a huge capillary barrier $\Delta P_{\text{total}} \approx 4\sigma/r \times$ number of lamellae, to change the pressure by an amount $4\sigma/r_0$ for each lamella. In a strong foam of size L, the number of lamellae $\propto L/r$ so $\Delta P \approx 4\sigma L/r^2$. Experimental values are significantly lower than this estimate [121,122]. Thus, the capillarity alone cannot explain the observed critical pressure drop. However, as shown above, more important is the ratio of pinning (capillary) forces to binding (elastic) forces, expressed as the parameter μ [Eq. (24)]. In the continuum model, the pressure variation is finite for all reasonable solutions (domain III in Fig. 16). The upper boundary for the maximum dimensionless pressure drop, G, is the maximum of the separatrix, i.e. the solution of algebraic equation,

$$\ln(1 + G) - G + \frac{2\mu}{K} = 0. \tag{33}$$

The bubble train is unable to sustain a pressure drop above G, if one of the train ends is free. The maximum external pressure rises as the bubble train acquires a

glass-like structure [114,115]. Determining the train ground state is difficult, because it depends on the pre-history of foam generation and motion.

Another significant experimental parameter is the ratio between the correlation length N_{cor} and the size of the sample, L, which determines finite-size effects. Even for small μK, when the continuum model holds, Eqs. (22), (27) and (28) show [115] that for $N_{cor} \gg L$, the critical pressure drop depends linearly on the number of lamellae in the train. In the dimensional form, the critical pressure drop $\overline{G}$ is:

$$\overline{G} = \frac{2\pi\sigma\delta}{Kr_0\lambda}N \tag{34}$$

The linearity of $\overline{G}(N)$ shows the independent contribution of each lamella to the total pressure drop. Similar behavior might be expected for the limiting case of absolutely compressible bubbles, for which the start-up yield pressure drop is completely determined by the overall Laplacian barrier. For an absolutely incompressible gas, the critical pressure drop is also linear.

For long samples, when $N_{cor} \ll L$, collective effects dominate and cause the screening effect: ahead of the domain wall lamellae stay undisturbed (see Fig. 17). The critical pressure drop corresponds to that required to form a domain wall in an infinitely long train, as in Eq. (32) [113,115]:

$$\overline{G} = 4\sqrt{\frac{P_g\sigma\delta}{r_0\lambda K}}\,. \tag{35}$$

The two limiting regimes [Eqs. (34) and (35)] demonstrate the importance of the size ratio. For short foams, the critical pressure drop depends on the sample length, regardless of foam texture and physical parameters. In Fig. 19, the experimental data reported by Falls et al. [121], their Table 2, are fitted to Eq. (34) ($G \propto r_b^{-3}$, r_b is the effective radius of a bubble), where the number of lamellae per unit length is inversely proportional to the volume of gas per bubble [44]. In the same picture, the expected result for a long train is presented as a dashed line ($G \propto r_b^{-3/2}$). Since the number of lamellae in the train was approximately eight, Eq. (34) adequately describes the experiment. The correlation length covers the entire bubble train.

Since glass-like ordering improves foam screening, determining the regimes of loading which result in a coarse-grained foam superstructure is desirable. This superstructure might be imagined as a random array of blocks with an internal crystalline-like order, separated by domain walls. In other words, the domain walls serve as apparent lamellae, and the blocks play the role of gas bubbles.

Another approach to determining the critical pressure drop takes the critical pressure drop as that required to keep lamellae moving by overcoming the capillary and viscous forces, which resist their advance [117,121,123–127]. Rossen [124–127] attributes a crucial role in the appearance of the critical pressure gradient to the sharp edges, or cusps, within a pore channel modeled as a tube with a periodically varying radius. For a piecewise linear distribution of pore radii, the channel is a

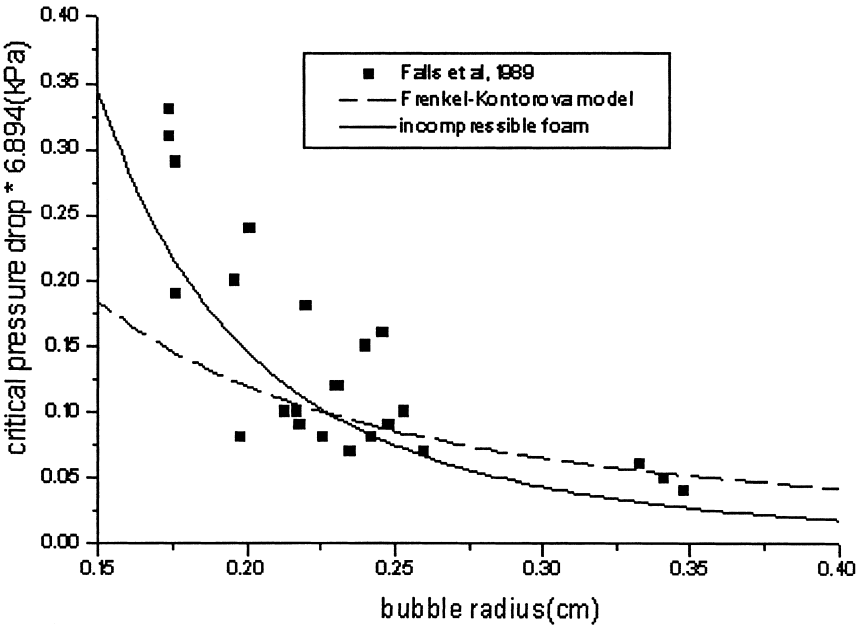

Fig. 19. The critical pressure drop as a function of the effective bubble radius.

series of frustums of cones. If the bubbles were incompressible, some lamella positions would be prohibited by geometric restrictions, and the lamella motion would become a sequence of alternating equilibrium positions. For certain shapes of the channel, e.g. with edges, or cusps, the bubble has to jump a certain distance in order to conserve volume during the motion. Jumps occur when the bubble volume becomes a non-monotonic function of the lamella position. To estimate the critical pressure gradient, we calculate the volume-averaged value of Laplacian pressure drop per bubble [121,123–127] (provided that bubble volumes are random and uncorrelated), which represents the net work required to push a lamella through a pore. The driving pressure is the time-averaged pressure drop per bubble. (For steady motion, the relation between the time and volume occupied by the bubble is linear). The critical pressure gradient in smooth inhomogeneous capillaries, e.g. sinusoidal, is zero, while in most experiments on homogeneous bead packs [121–123]), in which, active channels should be smooth, it is not.

Thus, both the experiment and theory cast doubt on the existing 'dynamic approach' to calculating the critical pressure drop. The critical pressure drop is hysteretic: to re-initiate flow, the 'yield' pressure drop has to increase above the initial level by 10–20% above that required to keep lamellae moving [128].

At least two different explanations are possible. Treating the foam as an elastic body, the critical pressure drop occurs when a dislocation deepens [110]. Equations of foam hydrodynamics, a solution of which determines an internal structure of the

foam, lead to a different critical pressure drop by considering the limit of infinitely slow flows.

3. Foam transport in smooth capillaries

Even above the critical pressure drop, when the foam flows, the gas flux is several orders of magnitude less than for pure gas [13,14,17,50,123,129]. Bretherton [130] explained the non-linear friction of a bubble as the result of competition between capillary and viscous forces. Later, Hirasaki and Lawson [44] and followers [121,131,50] extended the Bretherton approach to bubble train motion through smooth capillaries and bead packs. They implicitly assumed that foam motion resembles that of a single-phase system, with the joint motion of the gas, the liquid slugs separating the isolated bubbles, and the wetting film coating the pore walls, treated as pseudohomogeneous Darcy flow (relating the applied pressure gradient to the resulting flow rate). Within this approach, foam does not move relative to lamellae: all bubbles move *in unison*. However, the average velocities of different phases can be distinguished. In particular, the steady velocity of the gas bubbles is determined by the average velocity of the faster flowing fluid near the center of lamellae (or liquid lenses). Then, the volume swept out by a long bubble when moving with speed U equals the average speed U_{liquid} of the liquid, multiplied by the cross-sectional area of the tube. This balance estimate reveals that the average speed of the wetting fluid is less than the bubble velocity, U, by an amount WU, precisely, in the ratio $(1 - W) = (1 - h_\infty/R)^2$, where h_∞ is the thickness of the uniform film between the front and rear menisci and R is the pore radius (Fig. 20). Therefore, the smaller the film thickness, the smaller the difference in the average speeds of different phases. The average speed of the gas in bubbles slightly exceeds the average speed of the wetting fluid. Because of the large viscosity of the wetting fluid with respect to the gas viscosity, the resulting increase in apparent gas viscosity is expected to be appreciable.

Another scheme for foam flow in a capillary model is the wave-like motion of lamellae [113,132]. For each lamella in the train, the physical cause for lamella motion resembles that for a sailboat. Thus, the model is called the 'sailboat model'. The lamella, exerting a tensile force, draws a meniscus (the Plateau border) so that a lubrication flow occurs within the meniscus and the wetting film. As for Bretherton, the main flow patterns concentrate within the wetting film. Since the lamellar thickness, radius of curvature, and tension, all self-consistently depend on the changes of the wetting film, collective motion of lamellae cannot be predicted in advance. Stationary motion requires restrictions on the pressure distribution within the train.

Thus, the two models for foam friction appear to differ: the first deals with bubbles, while the second treats each lamella independently. The first considers the creep of the bubble train as a whole. The second treats motion as a wave-like displacement of lamellae in caravans.

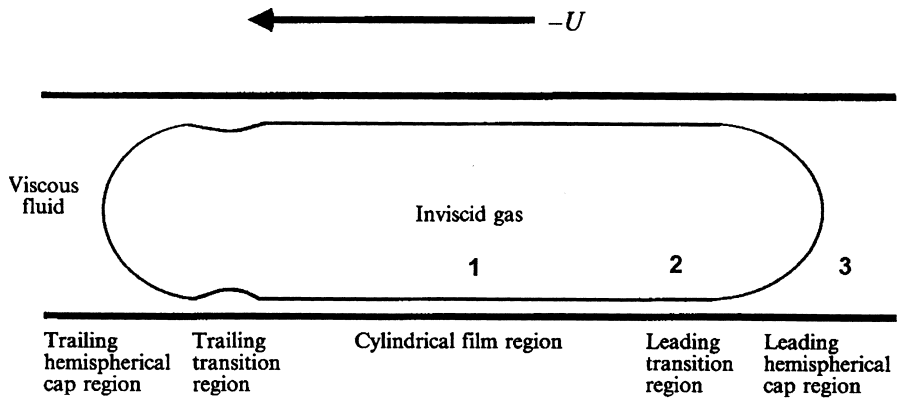

Fig. 20. Schematic of an air bubble traveling in the positive x-direction in a circular capillary.

3.1. The Bretherton mechanism of gas mobility reduction: motion of individual bubbles

Bretherton's [130] approach, which aimed at a simple description of bubble motion, obscures the physics of foam motion. It applies to many similar problems, e.g. the motion of drops [55,129,133–137] and some problems of dynamic wetting (the so-called Landatu–Levich problem [138–142]. In the literature on soap films, this problem is called the Frankel problem [2]. It diminishes the unique dynamic coexistence of the wetting film and foam lamellae.

For bubble motion *in unison* with the surrounding fluid, Bretherton invoked the lubrication approximation. Assuming that the gas viscosity is zero and the pressure within a bubble is constant, the volumetric flow rate is:

$$q = -\frac{h^3}{3\eta}\frac{\partial P_w}{\partial x}. \tag{36}$$

Here, η is the viscosity of wetting fluid, h is the wetting film thickness, and x is the spatial coordinate measured along the pore. At each point x, the pressure P_w across the film is assumed to be constant which depends on the film thickness as:

$$P_w = P_g - 2\sigma H. \tag{37}$$

Here, the effects of the disjoining pressure, which are important in sufficiently thin films, are ignored.

Thus, the flow within the film is controlled by a 'dynamic' capillary pressure and tends to establish a mechanical equilibrium between capillary and viscous forces, e.g. if the driving force is switched off, the bubble assumes a shape of constant mean curvature, as predicted by Eqs. (36) and (37).

The mass balance equation, written in the form:

$$\frac{\partial h}{\partial t} + \frac{\partial q}{\partial x} = 0, \tag{38}$$

completes the model. Eqs. (36)–(38) plus boundary conditions specify the physical situation. Bretherton considered steady motion of the bubbles and reformulated Eqs. (36)–(38) in a bubble fixed reference frame, $s = x - Ut$, where U denotes the speed of the bubble. He subdivided the steady profile of the wetting film at each bubble end into three regions (Fig. 20) within which different mechanisms determined the shape of the interface.

Where flow is slow, capillarity dominates the shape of the meniscus (region 3), so this region is designated as part of the equilibrium meniscus. Behind lies a uniform film (region 1), reached asymptotically. Between is the transition region 2, within which the film profile is governed by interplay of viscous and capillary forces. Assume that within region 2, the slope of the gas–liquid interface is small and the film thickness is much less than the pore radius. The interface shape in a bubble-fixed reference frame is

$$\frac{\mathrm{d}^3 h}{\mathrm{d}s^3} = \frac{3\eta U}{\sigma}\frac{h - h_\infty}{h^3}. \tag{39}$$

Here h_∞ is the 'asymptotic' film thickness in the middle part of the bubble. Transforming, $h \to h/h_\infty$ and $s \to s(3\eta U/\sigma)^{1/3}/h_\infty$, scales Eq. (39) so that the *capillary number* $Ca = 3\eta U/\sigma$ (which measures the ratio of viscous forces to capillary forces) and the 'asymptotic' film thickness do not appear explicitly:

$$\frac{\mathrm{d}^3 h}{\mathrm{d}s^3} = \frac{h - 1}{h^3}. \tag{40}$$

Bretherton numerically matched the thin film solution to the thick film solution at the ends of the bubble and assumed that the menisci have the curvatures equal to their static value (a modern numerical solution of autonomous third-order ordinary differential equations, like Eq. (40), is reviewed by Tuck and Schwartz [143]), i.e. he assumed, that equilibrium menisci exist and look like hemispherical caps. He did not assume that a film with uniform thickness h_∞, coexists with the menisci; the 'asymptotic' film thickness, h_∞ tends to zero with the capillary number, i.e. the equilibrium bubble consists of two hemispherical menisci and a segment of the dry tube, regardless of the wettability of the tube's surface! If the fluid wets the substrate completely, the Bretherton solution is not the asymptotic limit $Ca \to 0$, but an intermediate asymptote [144,145]. Nevertheless, the velocity of an individual bubble does slightly exceed the average speed of the fluid, U_{liquid}, by an amount,

$$W = \frac{U - U_{\mathrm{liquid}}}{U} = A\left(\frac{3\eta U}{\sigma}\right)^{2/3}, \quad A \approx 2.29, \qquad Ca = \frac{3\eta U}{\sigma} \to 0. \tag{41}$$

Bretherton also pointed out that the dynamic pressure drop across such a bubble, besides the Laplacian pressure drop:

$$\Delta P = B\left(\frac{3\eta U}{\sigma}\right)^{2/3}\frac{\sigma}{R}, \qquad B \approx 3.58 \tag{42}$$

Experimental results by Fairbrother and Stubbs [146] and Taylor [148] on an air–water system, flowing within circular tubes, indicated that, in the range of $10^{-4} < Ca < 10^{-2}$, the wetting film thickness was proportional to $Ca^{1/2}$, in contradiction to the Bretherton theory. (The Marchessault–Mason data also differ from the Bretherton predictions [147]).

Bretherton also experimented using aniline and benzene as the liquids. Theory and experiment disagreed for capillary numbers smaller than 0^{-4}. Schwartz et al. [149] in 1986 (see also [150]) repeated Bretherton's experiments, using water as the liquid phase (Fig. 21). The main parameters and Ca, were measured independently with high accuracy was expressed via the decrease in the length of the liquid slug AS and the distance of travel D as $W = \Delta S/D$. The capillary number was found by measuring the A-to-B travel time of the slug. The experimental findings are presented in Fig. 21d). As in the Bretherton experiments, the discrepancy between theory and measurements increases as the speed is reduced, where the asymptotic theory should work best. Explanations for the discrepancy between the theory and the experiment proposed in the literature include wall roughness [150], instability of the meniscus [130], intermolecular forces [55], and adsorbed impurities [55,130,151]. The action of impurities and the wall roughness is difficult to control. However, Ratulowski and Chang [151] disproved Chen's assertion that surface roughness causes the film thickness observed by Schwartz-Princen-Kiss. Teletzke [55] challenged the significance of intermolecular forces in the experiments. No simple hydrodynamics explains the Bretherton experiments, only an empirical treatment of the adsorption kinetics.

3.2. Modifications of the Bretherton theory: bubble train motion

Since the hydrodynamic picture of the flow within the Plateau border influences the resulting pressure drop very little, the Bretherton model applies to the case of touching bubbles. Hirasaki and Lawson [44] assumed that the bubble train moves like a piston so that the distance between the lamellae remains the same. The Plateau border is a region of constant curvature, i.e. the Plateau border is similar to the liquid ahead of and behind an isolated bubble, except that the radius of curvature of its meniscus can be less than the pore radius. The characteristic length of hydrodynamic perturbations becomes of order the size of the Plateau border, much smaller than the length of the bubble. Within uniform regions, the wetting film does not move but resides at the corresponding gas pressure P_i (see Eq. (37)). Because of the difference in the gas pressures within adjacent bubbles, the resulting pressure drop acts on the liquid, which flows from one bubble to another, 'bearing' the lamella. As a result, the total dynamic pressure drop per lamella

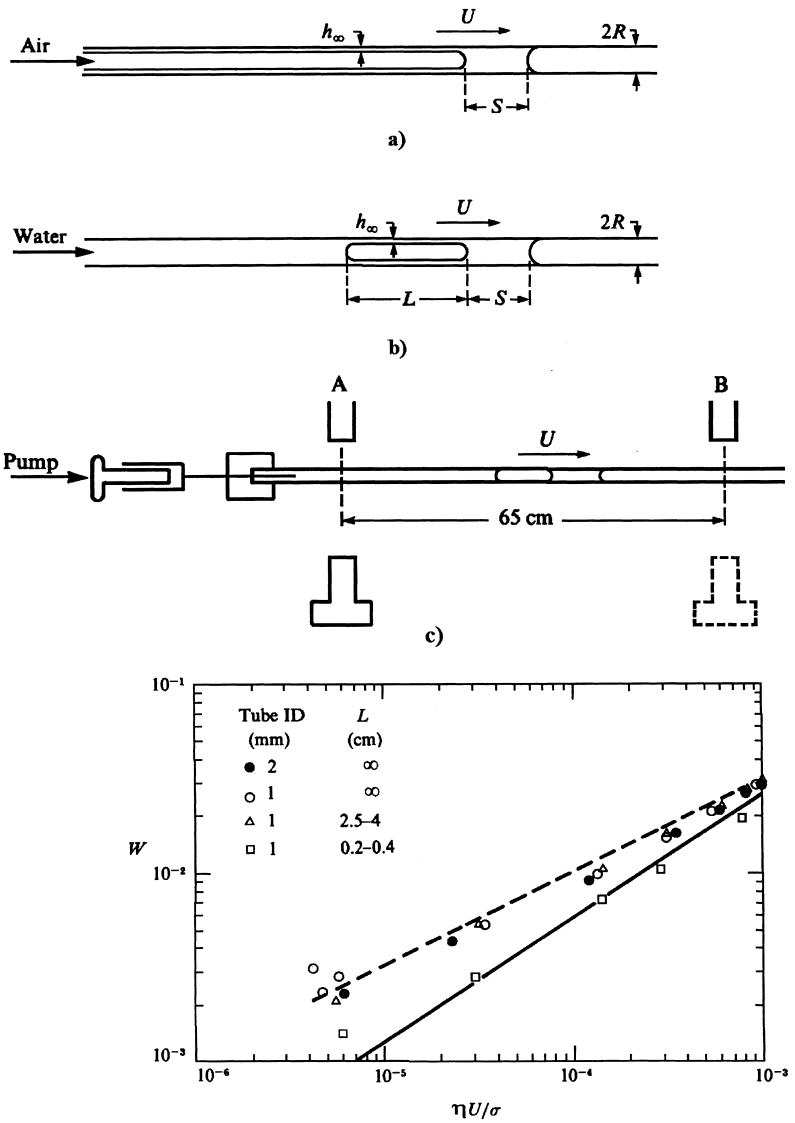

Fig. 21. (a) Endless and (b) finite air bubbles pushing a liquid slug. (c) Layout of experiment. (d) The variation in $W = 2h_\infty/R$ with capillary number: the solid line corresponds to Bretherton's theory. The dashed line shows the empirical correlation. $W = Ca.^{1/2}$ [149].

becomes proportional to $(Ca)^{2/3}\ \sigma/r_c$, where r_c is the radius of curvature of the interface at the Plateau border. Then, applying the Hagen–Poiseuille formula to the bubble train, the pressure drop can be compared with that required to maintain steady flow of the wetting fluid within the same pore at the same average speed. The apparent viscosity of foam relative to the liquid, or the ratio of the respective

pressure drops, is of order $NCa^{-1/3}$ where N is the number of lamellae in the train. For typical reservoir conditions, $Ca \approx 10^{-6}$ to -10^{-3} hence the apparent viscosity of foam is a factor of 10–100 N larger than for pure liquid.

Ratulowski and Chang [131], using the same Eq. (40), extended the Hirasaki–Lawson results by accounting for the difference in the radii of curvature for the forward and backward menisci. Their numerical study, verified by matched asymptotic expansions, showed that at low capillary numbers the pressure drop across each bubble in the train is identical to that of an isolated bubble [Eq. (42)]; where the radius of the Plateau border, r_c, is used instead of R). That is, the bubbles in the train do not 'feel' one another when the train creeps as a whole through the pore. The result is more apparent than real, because the model employed neglects many physical processes at the contact line. The hydrodynamic picture of the flow within the Plateau border is quite complex. However, Park and Homsy [152] showed theoretically that the integral characteristics of the flow, such as the total pressure drop and the 'asymptotic' film thickness, are appropriately predicted by the Bretherton theory. The next contribution to these integral characteristics would be of order of $O(Ca)$ [152].

On the other hand, in the range of capillary numbers appropriate for the Bretherton theory, $Ca > 10^{-4}$, Hirasaki and Lawson [44] experimentally showed that the pressure drop per bubble exceeds the Bretherton prediction by about one order of magnitude. They attributed the discrepancy to the effect of the surface tension gradient.

Recall that the surfactant is adsorbed along the fluid interfaces, where it lowers the interfacial tension. Convection reduces the surfactant concentration at the front of the bubble and increases its surface concentration near the stagnation zone where the flow converges. Adsorption–desorption and the bulk diffusion diminish gradients in surface concentration, and, if either of these fluxes are low, a non-uniform distribution of the adsorbed surfactant causes a gradient in the interfacial tension. The resulting *Marangoni stress* [139] is directed from regions of lower surface tension toward regions of higher tension and causes interfacial convection.

Herbolzheimer [153] and Chang and Ratulowski [151,154] demonstrated theoretically that the upper estimate for the film thickness and the pressure drop resulting from the Marangoni effect is $4^{2/3}$ times the Bretherton expressions (Hirasaki and Lawson [44] took these constants as fitting parameters). Studies on the behavior of soluble surfactants at various convective, diffusive and sorptive kinetic timescales [151,155] and the bubble length [156], indicate that the pressure drop for long bubbles are always bounded by a maximum predicted by the Herbolzheimer–Chang–Ratulowski model. Thus, this effect cannot explain the experimental results of Hirasaki and Lawson. In biological applications, another type of 'dynamic' screening by foam could play an important role, the flexibility of channel walls [157]. A moving bubble creates convergent and divergent regions. which lead to a critical pressure drop. The start-up pressure drop must be distinguished from that required to keep the foam moving, as in Section 2.9. Gaver et al. [158] in the spirit of the Bretherton theory, demonstrates that the critical 'dynamic' pressure drop

required to keep the bubble moving steadily corresponds to the lower boundary for admissible pressure drops and serves as a solvability condition for the Bretherton traveling-wave solution. Gaver et al. [158] termed this critical pressure drop, the start-up, yield–pressure drop.

Thus, the Bretherton theory includes a number of different physical effects, but, because of its asymptotic character, does not elucidate the interaction between the lamella itself and the flowing liquid within the Plateau border. It implies that each lamella in the train moves steadily, which is only one possible scenario of lamellar motion. Other schemes, e.g. motion of lamellae with acceleration, or with formation of a ring vortex in the Plateau borders [45] are possible. However, to describe these flows, a rigorous mathematical formulation of the problem is needed.

3.3. Sailboat model

As discussed in the previous sections, the line of contact of the lamella and the wetting film plays a role of a three-phase contact line. During motion, all geometrical parameters, such as the lamella thickness, the wetting film thickness, the inclination angles and the curvatures of the menisci at the Plateau border, are mutually consistent. Recall that at thermodynamic equilibrium, contact conditions, e.g. 'free film–wetting film', can be found by applying ordinary thermodynamic rules. However, hydrodynamics also plays an important role, since the lamella exerts a time-dependent tensile force on the wetting film surface. Therefore, the determination of the shape of the moving wetting film is a free boundary problem. We have to find two functions — the thickness of the wetting film behind and ahead of the contact line, and the time-dependent coordinates of the contact line, by accounting for the coexistence conditions of the free and wetting film.

To approximate the Bretherton approach, we use the lubrication approximation [Eq. (36)]. However, in order to guarantee the existence of the equilibrium wetting film at the pore wall, we modify Eq. (37) by introducing the disjoining pressure $\Pi_w(h)$ via the equation,

$$P_w = P_g - 2\sigma H - \Pi_w(h). \tag{43}$$

Recall that $2H$ is the curvature of the interface. For a flat substrate (i.e. in the asymptotic limit $h/R \to 0$, where R is the pore radius):

$$2H = \frac{\mathrm{d}^2 h}{\mathrm{d}x^2}\left(1 + \left(\frac{\mathrm{d}h}{\mathrm{d}x}\right)^2\right)^{3/2}. \tag{44}$$

Thus, Eqs. (36), (38), (43) and (44) describe two film profiles h_i and h_{i+1} associated with the i-th and $(i + 1)$-th bubbles of the train. These functions have to match at the three-phase contact line. The free boundary, i.e. at the three-phase contact line, has five boundary conditions, because the curvature in Eqs. (43) and (44) is expressed through the second derivatives of the fields, and Eqs. (36) and (38) give two additional derivatives.

3.3.1. Continuity condition

The first boundary condition is the continuity condition:

$$h_i|_{x\to\xi-0} = h_{i+1}|_{x\to\xi+0} \tag{45}$$

where ξ is the coordinate of the contact line.

3.3.2. Force balance

Local mechanical equilibrium gives the second boundary condition, with restrictions dictated by the geometry.

Denote $_i$ as the inclination angle between the lamella and the i-th air-wetting fluid interface (Fig. 22). Then the angle between the interfaces i and $i+1$ will be:

$$= 2\pi - \alpha_i - \alpha_{i+1}. \tag{46}$$

Since the profile of the i-th film is increasing, while h_{i+1} decreases with x, the angle can be expressed as;

$$\theta = \beta_{i+1} - \beta_{i,}\ \tan\beta_i = \left.\frac{\partial h_i}{\partial x}\right|_{x=\xi}. \tag{47}$$

Thus, Eqs. (46) and (47) connect the inclination angles with the first spatial derivative, i.e. the slope of the film profile at the contact line. On the other hand, the inclination angles depend upon the lamella tension, as follows from the conditions of mechanical equilibrium:

$$\gamma_d = \sigma_i\cos(\pi - \alpha_i) + \sigma_{i+1}\cos(\pi - \alpha_{i+1}) - F_{\|}, \tag{48}$$

$$F_{\perp} + \sigma_i\sin(\pi - \alpha_i) = \sigma_{i+1}\sin(\pi - \alpha_{i+1}), \tag{49}$$

where γ_d is the dynamic tension of the lamella and $_i$ is the surface tension of the wetting film in the i-th bubble. A specific friction of the contact line causes the extra-force $F(F_{\|}, F_{\perp})$. The latter is unknown beforehand and must be found. Generally speaking, the surface tensions in adjacent bubbles can be distinguished by virtue of different 'dynamic' concentrations of the surfactant. But if we neglect

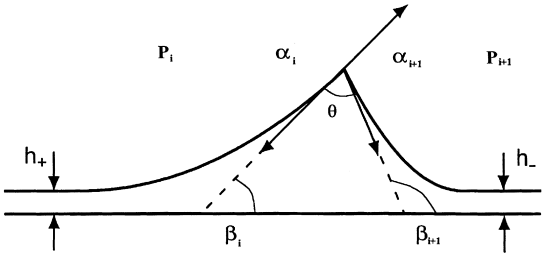

Fig. 22. Schematic of a lamella sliding over a wetting film.

this concentration effect, the surface tensions in different bubbles become equal to one another. As shown in Section 2.6, the equilibrium lamella tension is a function of the film thickness. However, the 'dynamic' lamella tension differs from its thermodynamic value because of flow occurring within the lamella.

3.3.3. Lamella thickness and dynamic tension

To demonstrate the effect of dynamic tension, we assume for simplicity that during the motion, the lamella bulges uniformly like a spherical cap. We also assume that the lamella does not change its volume, but fluid redistributes over a new area by an elongation flow.

The first assumption permits a description of the flow in spherical coordinates. The second assumption imposes a diagonal stress tensor with non-zero components, in addition to the hydrostatic pressure, τ_{rr}, $\tau_{\theta\theta}$, $\tau_{\varphi\varphi}$. Together all tensor components are r-independent functions of the film thickness. Following Section 6 instead of Eqs. (10) and (12), we write the balance of normal stresses at both outer lamella surfaces as:

$$-\left(P_i + \frac{2\sigma}{R_{ii+1}}\right) + \Pi(h_{ii+1}) = -P_w + \tau_{rr}, \tag{50}$$

$$-\left(P_{i+1} - \frac{2\sigma}{R_{ii+1}}\right) + \Pi(h_{ii+1}) = -P_w + \tau_{rr}. \tag{51}$$

Eqs. (50) and (51) give the mean radius of the lamella from the ordinary Laplace equation such as Eq. (13), with the lamella tension and the pressure difference in Eq. (13) treated as dynamic values, because they differ from the equilibrium values by an amount lost due to lamella motion. Eq. (13) describes the motion of individual lamella, provided that the radius R_{ii+1} is expressed through the lamella chord radius, $R - h_i(\xi)$, and the apparent contact angle ψ as:

$$\frac{\sin\psi}{R - h_i(\xi)} = \frac{1}{2\sigma}(P_{i+1} - P_i) \tag{52}$$

Eqs. (50) and (51) relate the lamella thickness, the disjoining pressure and normal stress as:

$$\Pi(h_{ii+1}) = \tfrac{1}{2}(\Delta P_{i+1} + \Delta P_i) + \tau_{rr}, \qquad \Delta P_i = P_i - P_w(\xi,t). \tag{53}$$

At this step, the rheological model for the lamella has to be specified. To date, no conventional rheological model for foam lamellae exists, because the structure of the foam films remains enigmatic. A smectic-like structure [37,159], a cubic lattice of ordered micelles [160], a fluid with a specific exponential correlation function [170], a bilayer of surfactants with aqueous core [161,162] and a gel-like structure [163–165] are only a few of the possible structures, each requiring a

specific approach to the rheology. Specific surface properties of the foam films also modify rheological relations [166–169], so designating the form of the normal stress is difficult.

Nevertheless, many rheological laws permit the expression of the normal stress, τ_{rr}, in terms of the extensional strains rates, e_{rr} and $e_{\varphi\varphi}$. Due to the definition, they are $e_{rr} = \mathrm{d}\ln h_{ii+1}/\mathrm{d}t$, $e_{\varphi\varphi} = \mathrm{d}\ln(R - h_i(\xi))/\mathrm{d}t$. Then the normal stress, τ_{rr}, can be expressed through the time derivative of the lamella thickness and chord radius. For instance, assuming that the lamella deforms as a Newtonian fluid, we have the linear relation between the respective component of the stress tensor and the extensional strain rate, i.e. $\tau_{rr} = \eta_l\, \mathrm{d}\ln h_{ii+1}/\mathrm{d}t$, where η_l is the lamella viscosity.

Thus, the lamella thickness implicitly depends upon the dynamic pressure drop, the magnitude of the pressure within the lamella and the height of the crest. However, the pressure within the lamella must be equal to the pressure in the wetting fluid. Eq. (53) relates the parameters of the wetting film and the lamella thickness. Therefore, giving the functional form of the disjoining pressure, the lamella thickness can be found at any instant of time as a function of the input parameters by solving Eq. (53).

Finally, the dynamic tension of the lamella can be found from the balance of tangential forces assuming that the film surface tension is approximated by Eq. (10) for flat films:

$$\gamma_d = 2\sigma + \int_{h_{ii+1}}^{\infty} \Pi(h)\mathrm{d}h - h_{ii+1}(P_w(\xi) - P_{i+1}) + h_{ii+1}\tau_{\theta\theta}. \tag{54}$$

Here we choose $h_{ii+1}P_{i+1}$ as a 'reference or background tension'. Substituting the difference $(P_w(\xi) - P_{i+1})$ from Eq. (51) into Eq. (54) and omitting the term of order h/R, we arrive at the formula for dynamic tension:

$$\gamma_d = \gamma + h_{ii+1}(\tau_{\theta\theta} - \tau_{rr}). \tag{55}$$

The above analysis demonstrates how the lamella rheology influences its dynamic tension, e.g. for a Newtonian fluid, the theta-component of the stress tensor is a linear function of the respective component of the extensional strain rate, $e_{\theta\theta}$. Due to fluid incompressibility, $e_{\theta\theta}$ is a function of the two others, i.e. $e_{\theta\theta} = -e_{rr} - e_{\varphi\varphi}$, and can be expressed through the film thickness and the lamella radius.

All the lamella parameters, such as thickness, apparent contact angle and tension, are self-consistently connected with the wetting film parameters.

3.3.4. Pressure continuity

The lubrication approximation implies that the pressure in the wetting fluid at the contact line varies continuously. Making use of Eq. (43), the desired boundary condition is written as:

$$P_i - 2\sigma H\,|_{x\to\xi-0} = P_{i+1} - 2\sigma H\,|_{x\to\xi+0}. \tag{56}$$

3.3.5. Mass balance

The last boundary condition is the balance of local mass fluxes at the moving boundary: if the lamella is passing the distance $d\xi$ for the time interval dt, the mass change, on the one hand, is $(h_i(\xi) - \min(h_i, h_{i+1})|_{|x|\to\infty})d\xi$ and, on the other hand, this change is the flow influx $q\,dt$. Hence the boundary condition is,

$$\left(h_i(\xi) - \min(h_i,h_{i+1})|_{|x|\to\infty}\right)\frac{d\xi}{dt} = q|_{x\to\xi-0}, q|_{x\to\xi-0} = q|_{x\to\xi+0}. \tag{57}$$

Here $h_i|_{x\to-\infty}$ is the thickness of the film at infinity, an unknown parameter, so Eqs. (36), (38), (43) and (57) are subject to additional boundary conditions at the ends of the wetting films. At the end where the film remains at rest, the film thickness has a well-defined value. At the same time, the thickness of the residual film at the opposite end is unknown and has to be found. We assume that all the spatial derivatives at both ends vanish, i.e. the wetting films tend to be flat at the ends. Also, we have to presume some law for fluid depletion in the system 'lamella + wetting film'

3.4. Sailboat model: traveling wave solution

The model formulated in the previous section constitutes the basis for a self-consistent theory of lamella residence and motion. We demonstrate its characteristic features by analyzing the traveling-wave solution of form,

$$h = h(s), \qquad s = x - Ut,$$

where is the velocity of the lamella propagation over the wetting film. This solution can describe the steady motion of an individual lamella over the prewetted pore, as well as the steady motion of the i-th lamella of a bubble train, when the latter is moving as a whole.

The first integration of the governing equations with respect to S, leads to:

$$-\frac{3\eta U}{h_m^3}(h_m - h^{\pm}) = \frac{d}{ds}P_w(h_m), \qquad m = i,i+1, \tag{58}$$

where '+' is the film thickness at left infinity and '−' at right infinity. The integration of Eq. (58) relates between the pressure drop and the lamellar speed

$$-3\eta U\left(\int_{-\infty}^{0}\frac{h-h^+}{h^3}ds + \int_0^{\infty}\frac{h-h^-}{h^3}ds\right) = -P_i + P_{i+1} + \Pi_w(h^-) - \Pi_w(h^+). \tag{59}$$

On the other hand, the mass balance, Eq. (57), reveals that the residual film thickness and the film thickness at right infinity are the same, $h^+ = h^-$. At low speed, the displacement can be classified as quasi-static, and the film profile is governed by the capillary and the disjoining pressures. The residual film thickness

h^+ and the apparent contact angle θ have essentially the same values as if the meniscus was motionless, $h^+ = h^- \approx h_\infty$, where h_∞. is the equilibrium film thickness at infinity. As a result, to leading order in U we have the linear (Newtonian) friction law:

$$\frac{3\eta_{app}U}{h_\infty} = \Delta P, \tag{60}$$

where ΔP is the dynamic pressure drop for a steadily moving lamella. The apparent viscosity, η_{app}, is expressed through the thermodynamic parameters of the equilibrium film as:

$$\eta_{app} = 2\eta\int_0^\infty \frac{H-1}{H^3}\mathrm{d}X, H = \frac{h}{h_\infty}, \quad X = \frac{x}{h_\infty}. \tag{61}$$

In particular, for the Derjaguin–Landau approximation to the disjoining pressure [171], $\Pi_w = A/h^2$, $A = 2.36 \times 10^{-12}$ J m^{-2}, the equilibrium shape of the Plateau border can be described analytically [91]. Therefore, the apparent viscosity can be completely investigated as a function of the physical input parameters. For ordinary black films, the contact angle $2\theta_0$, is very small [8,9], even vanishing. Then the principal term in the asymptotic expansion of the apparent viscosity with respect to $\beta_{DL} = A/\sigma h_\infty \ll 1$, has the form [172]:

$$\frac{\eta_{app}}{\eta} \propto \frac{1}{\sqrt{\beta_{DL}}} + O\left(\sqrt{\beta_{DL}}\right). \tag{62}$$

The thicker the equilibrium film, the greater the apparent viscosity of the foam. Since the equilibrium film thickness is indissolubly connected with the size of the Plateau borders, the growth of the film thickness implies an increase in the size of the Plateau borders. Therefore, the bigger the border, the greater is the effective frictional area. The same tendency might be expected for other forms of the disjoining pressure isotherms because the transition zone makes the main contribution to the apparent viscosity of a lamella. However, the overall foam resistance increases when the foam becomes dryer. For example, substituting Eq. (62) into Eq. (60), we arrive at the following scaling relation $\Delta P \propto U/\sqrt{h_\infty}$. A linear relation between the pressure drop and the lamella velocity has been observed, but not explained by Nutt and Burley [45].

The two limiting regimes of the lamella friction are Newtonian friction and non-Newtonian friction (the power-law Bretherton model). The Bretherton regime selects a unique film thickness, over which the lamella can only propagate steadily, with no other traveling-wave solutions [131]. As the displacement speed increases, the apparent contact angle between the substrate and bubble interface decreases to zero, when a visible film is deposited, regardless of the wettability of the surface [55,173]. A similar change of regimes of motion might be expected for foam

lamellae as well, but remains an open question. A detailed experimental analysis of foam motion in smooth capillaries at low capillary numbers, $Ca < 10^{-4}$, is highly desirable.

4. Flow trough bamboo-like capillaries and porous media

4.1. Lamella in bamboo-like capillaries: stick-slip motion

In the previous sections, we discussed resistance to creeping during steady lamella motion with a constant speed. Creeping occurs only in smooth capillaries. Any wave-like irregularity of the channel produces an additional Laplacian force, which is non-monotonic with respect to spatial coordinates, resulting in an irregular motion of a lamella. After the lamella leaves the pore throat, it bulges forward and resists movement. In the pore enlargement, the lamella bulges backward and accelerates. Visual experiments [46,48] reveal that, when pushed at a constant pressure drop, often the lamellae exhibit stick-slip motion [174,175].

The stick-slip motion can be qualitatively described by using the following model:

$$m\frac{\mathrm{d}^2\rho_i}{\mathrm{d}\bar{t}^2} = \pi r_0^2 \Delta P, \tag{63}$$

where m is the effective mass of the lamella, $\bar{t}$ is the dimensional time, and ΔP is the pressure drop across the lamella, from the Laplacian pressure drop, Eq. (13), the dynamic pressure drop, Eqs. (42) and (60), and the external pressure drop. Consider a quasi-static motion so that all deviations from Newtonian friction are small. As in Sections 2.6–2.9, we assume that the lamella intersects the pore walls at 90°, in dimensionless variables, Eq. (63) takes the form:

$$\varepsilon^2\frac{\mathrm{d}^2\rho_i}{\mathrm{d}t^2} + \frac{\mathrm{d}\rho_i}{\mathrm{d}t} = \Delta p - 2\pi\mu\sin\rho_i, \tag{64}$$

where $\varepsilon^2 = 2mh_\infty^2 P_g/9\eta_{\mathrm{app}}^2 r_0^2\lambda$ and the dimensionless time is $t = 2\pi h_\infty P_g \bar{t}/3\lambda\eta_{\mathrm{app}}$. Δp is the external pressure drop scaled by P_g. Eq. (64) has a very broad range of interpretations, depending on the choice of parameters [111,112,176,177]. In lamella motion, ε is usually small, so the first term in the left hand side of Eq. (64) dominates the second only for short times. At long times, the inertial term may be dropped and Eq. (64) takes the form:

$$\frac{\mathrm{d}\rho_i}{\mathrm{d}t} = \Delta p - 2\pi\mu\ \sin\rho_i, \qquad \Delta p = \mathrm{Const}. \tag{65}$$

This equation has an analytic solution [178] (see also [111]),

$$\rho(t) = 2\tan^{-1}\left[\left(\frac{\Delta p^2 - 4\pi^2\mu^2}{\Delta p^2}\right)^{1/2}\tan\left(\frac{\pi t}{T}\right) + \frac{2\pi\mu}{\Delta p}\right], \tag{66}$$

where the period T is

$$T = \frac{2\pi}{\sqrt{\Delta p^2 - 4\pi^2\mu^2}} \tag{67}$$

The characteristic time for translation over a period of the channel depends upon the applied pressure drop.

Thus, the periodic motion represented by Eq. (66) looks like stick-slip motion. In the vicinity of a threshold, i.e. when the applied pressure drop is of the same order as the Laplacian barrier, $\Delta p \approx 2\pi\mu$, the lamella spends most time in a slow creep. After overcoming the maximum pinning force (i.e. after reaching the point $\rho = \pi/2$), the lamella suddenly jumps over an enlargement and the motion repeats itself. As the pressure drop increases, the jump time becomes negligibly small, and the lamella moves almost steadily. The lamella velocity, averaged over the period T, becomes a non-linear function of the external pressure drop:

$$\langle\dot{\rho}\rangle = \frac{1}{T}\int_0^T \frac{\mathrm{d}\rho}{\mathrm{d}\tau}\mathrm{d}t = \frac{2\pi}{T} = \sqrt{\Delta p^2 - 4\pi^2\mu^2}\,, \tag{68}$$

with the expected threshold $\Delta p \approx \mu$. Eq. (68) displays an increase of the apparent viscosity of the lamella with increasing rate of shear, as determined by the lamella speed (Figs. 23 and 24), 'shear-thickening' [179]. The averaging which leads to Eq. (68) somewhat disguises its cause: near the vicinity of the critical pressure drop, capillary forces drive the lamella almost entirely. In this critical regime, a 'bare' external pressure drop is needed to compel the lamella to shift from its equilibrium position. Once shifted, the lamella drifts almost autonomously. Only in a high-speed regime does the apparent viscosity of the lamella tend to its bare value.

Therefore, this 'shear thickening' behavior of a lamella is caused solely by irregularities of the channel. If we increase the pressure drop further and further, we inevitably arrive at the range of validity of the Bretherton theory. In this flow regime, 'shear thickening' behavior can change to the 'shear-thinning' (i.e. the reduction of viscosity with increasing rate of shear in an averaged steady flow) [113]. One possible explanation of the experimentally observed 'shear thinning' (Fig. 25) is the non-linearity of the friction law as expected from the Bretherton theory [121], though the theory, which deals with a uniform capillary and which diminishes the effect of gas compressibility, underestimates the foam viscosity under all experimental conditions (Fig. 26), and incorrectly predicts dependence of the gas phase velocity.

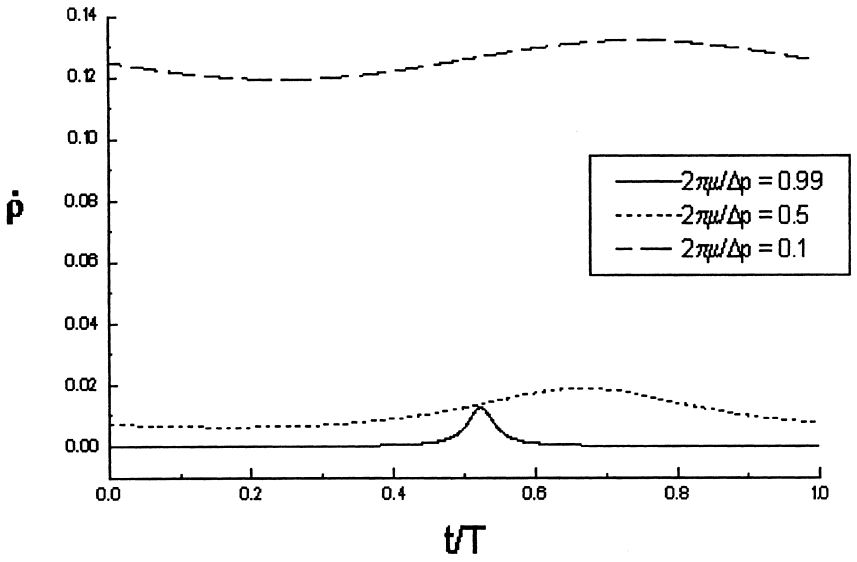

Fig. 23. Transition from a stick-slip motion to a sliding motion [Eqs. (66) and (67), $\mu = 10^{-3}$).

To resolve the contradictions, Falls et al. [121] modified the Hirasaki–Lawson theory to account for the contribution of pore constrictions to the apparent viscosity. They approximated the Laplacian contribution to the dynamic pressure gradient as $\nabla P \approx n_l\, 4\sigma/r_t$, where n_l is the number of lamellae per unit length and

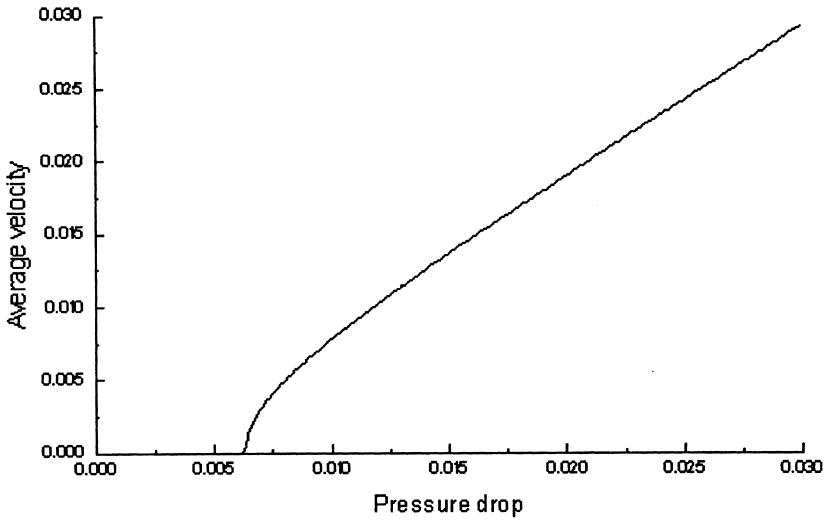

Fig. 24. 'Shear-thickening' behavior of an individual lamella. The increase of viscosity with the increasing rate of shear in an averaged steady shear flow [see Eq. (68), $\mu = 10^{-3}$].

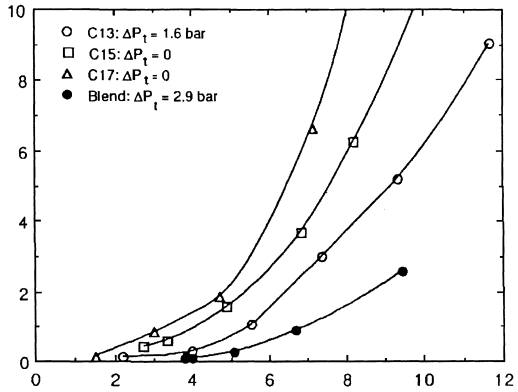

Fig. 25. Typical rheological curves. Foams from 0.25% Hostapur SAS carbon number fractions. The length of the pack, 100 cm; the permeability, 8 darcy; the pressure at the exciting end, 7 bar. ΔP_t, denotes the threshold pressure drop; vertical axis, the gas flow rate (ml min^{-1}); horizontal axis, the pressure drop/the length of the pack (bar m^{-1}) [122].

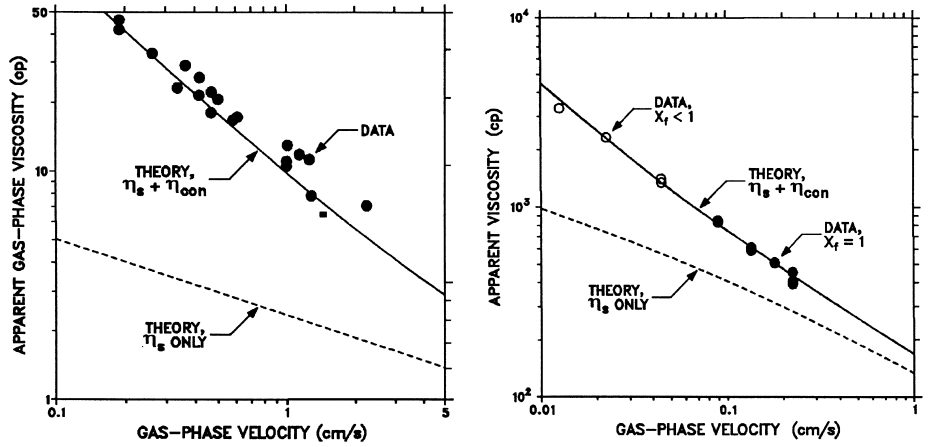

Fig. 26. Apparent foam viscosity in glass bead packs as a function of gas-phase velocity. Physical conditions: the capillary pressure $P_c \approx 1900$ dynes cm^{-2}; the ordinary gas-phase relative permeability, $k_{rg} \approx 0.056$. (a) The controlled-bubble-size regime, $r_b / r_{cap} \approx 3.8$, where r_b is the effective radius of a foam bubble and r_{cap} is an equivalent capillary radius. (b) The pack-generated bubble-size regime, $r_b/r_{cap} \approx 0.92$. The parameter $X_f = S_{gf}/S_g$ is the ratio of the moving-gas saturation S_{gf}, estimated from the measured residence time of flowing gas, and the gas saturation, S_g. For the pack-generated bubble-size regime, $X_f = 1$; η_s, is the Hirasaki–Lawson viscosity [121].

r_t is the radius of the pore throat. As a result, the Laplacian contribution augments the Hirasaki–Lawson apparent viscosity defined through the Hagen–Poiseuille law as, $\eta_{con} \approx 4\sigma n_l / v_g r_t$, where v_g is the gas-phase velocity. Thus, the apparent viscosity must vary with the -1 power of the gas velocity at low speeds. Falls and

coworkers studied two regimes of foam generation: so-called controlled-bubble-size regime, where the bubble size was unchanged in situ, and the liquid was transported within the lamellae; and the so-called pack-generated-bubble-size regime, where one bead pack was used to generate the foam for a second. For both flow regimes the apparent viscosity measured at low speeds varies as -1 power of the gas-phase velocity. The authors fit the Hirasaki–Lawson theory to the experimental data even at higher speeds. At higher rates, the viscosity varies as the $-1/3$ power of the velocity in the first flow regime, and changes to the $-2/3$ power of the velocity in the second, so the surface tension gradient governs the foam resistance in the second flow regime [44] (see also Section 3.2).

Thus, the key assumption in treating the experimental data is the contribution of the pore constrictions to lamella resistance, which determines the changes in apparent viscosity as a function of the gas velocity. The results apply only for capillary numbers $10^{-4} < Ca \ll 1$ and for short bubble trains, when the length of the sample is of the order of magnitude of the correlation length N_{cor} of the train. (The Falls–Musters–Ratulowski experiments fall into this range, see Section 2.9). Otherwise, the chain elasticity cannot be ignored and modifies the theory.

4.2. Stick-slip motion of bubble trains

Consider waves caused by oscillations of gas pressure within bubbles [113,132], which apply to acoustic flows, for which the high frequency modes are important, and transport of bubble trains. We first consider the propagation of acoustic waves through a perfectly ordered one-dimensional foam, i.e. through a bubble chain.

We first specify the dispersion relations [116]. For the linearized version of Eqs. (64) and (20), the dispersion relation has the form (neglecting the lamella friction):

$$\omega^2 = \omega_0^2\left(\sin^2\frac{K\lambda k}{2} + 2\pi^2 K\mu\right), \qquad \omega_0^2 = \frac{2P_g}{\rho_{\mathrm{liquid}} hK\lambda}, \tag{69}$$

where ω is the frequency, k is the wave number, and h is the lamella thickness. Eq. (69) has two critical frequencies, below and above which acoustic waves will not propagate through the chain. The lower critical boundary corresponds to the natural frequency of the individual lamella, reached when the wavelength tends to infinity (or $k \to 0$), i.e. when the bubble train oscillates as a whole, and when all the lamellae vibrate at the throats of pore channels *in unison*. Another critical frequency selects the range of wave numbers allowed by the theory (when the wavelength becomes comparable with the distance between adjacent lamellae, the theory fails to describe the triple substrate–gas–lamella interactions). The theory does not require pore channels with small pore aspect ratios, but is valid for all channels with perfectly ordered foam.

Because screening originates from the Laplacian blocking action of the lamellae, we expect that any perturbation will be suppressed if its frequency lies outside the allowed range. Our analysis applies only to waves of small amplitude, and cannot be extended directly to the non-linear case. For the stick-slip motion of lamellae,

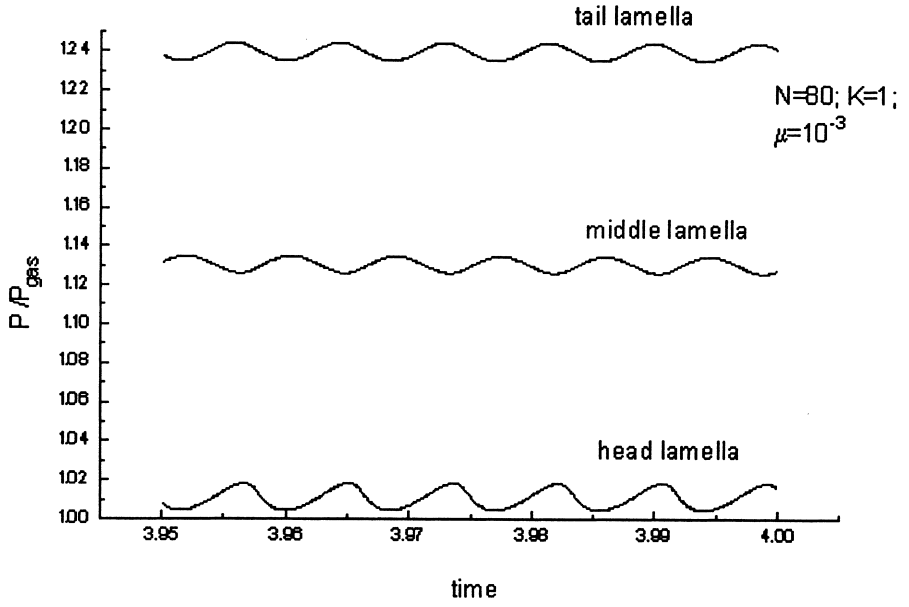

Fig. 27. Wave motion of foam. The head and tail lamellae move *in unison*, while the middle lamella moves in antiphase. Numerical experiment based on Eq. (64) and Eq. (20), $\varepsilon = 0$ [180].

we should focus on the wave-propagating solutions of the non-linear model, Eqs. (64) and (20), which dynamics occurs when we excite just one lamella, with all others initially at rest.

In its general features, the stick-slip motion of the lamellae resembles the Frenkel–Kontorova mechanism for the flow of dislocations in crystals [107]. The excited lamella initiates a wave propagating through the bubble chain in a 'falling dominos' type of motion towards the other end of the chain, which is then reflected, moving in the opposite direction towards the initially excited lamella (Fig. 27). In such a motion, practically no energy is lost during the flow, because the surface energy of the lamellae is compensated almost entirely by the elastic energy of the bubbles.

Focusing on the short time dynamics within an interval, we find a solution like the Frenkel–Kontorova kink [107,181,182]. Just after the external pressure drop has overcome the threshold $\overline{G}$ [Eqs. (33) and (35)], the domain wall, which separates the stagnation zones ahead of and behind the front of the wave, deepens and runs forward. Therefore, in soliton dynamics, the competition between the inertial, elastic, and pinning forces is important, and the viscous forces do not crucially change the character of the soliton propagation over short periods. If a bubble train moves for a long time, the inertial forces are negligibly small with respect to the three major forces — the elastic, viscous, and capillary forces. These forces together drive the displacement waves. If the external pressure drop is maintained for a long time, the number of the domain walls increases proportio-

nally to the number of channel periods over which the front domain wall has skipped. Therefore, the longer the bubble train, the greater the number of domain walls, and, consequently, the greater the bubble train resistance.

To illustrate collective effects in bubble train friction, we use a simplified model of lamellar interactions. A linear elastic spring represents the elastic interactions of the lamellae. Because each individual domain wall plays a role in the chain friction, we focus on the motion of a solitary wave. Then, in the continuum limit, Eq. (65) is [113]:

$$\frac{\partial \rho}{\partial t} = \frac{\partial^2 \rho}{\partial s^2} - \frac{\mu}{K}\sin\rho + \Psi. \tag{70}$$

Here Ψ is a dimensionless external force which represents the total action of the external pressure gradient on each lamella in the chain. In the vicinity of the threshold, the profile of a domain wall can be adequately approximated by Eq. (32), provided that the condition $G \approx \sqrt{\mu} \ll 1$ holds. Then, rewriting Eq. (70) in a wave-fixed reference frame, the velocity of the domain wall is found as the solvability condition to Eq. (70) [113,183],

$$-v\int_{-\infty}^{\infty}\left(\frac{\mathrm{d}\rho}{\mathrm{d}x}\right)^2 \mathrm{d}x = \Psi\int_{-\infty}^{\infty}\frac{\mathrm{d}\rho}{\mathrm{d}x}\mathrm{d}x, \tag{71}$$

where $x = \sqrt{\mu}(s - vt)$ and the function ρ in Eq. (71) is expressed by Eq. (32). Substituting Eq. (32) into Eq. (71), we have:

$$v \propto \frac{\Psi}{\sqrt{\mu}}. \tag{72}$$

Thus, Eq. (72) may be treated as an equation for the motion of effective individual lamellae along an active channel. The friction coefficient of such a macro-lamella is affected by the binding and pinning energies of the chain. Braiman–Family–Hentschel [184] and Musin's [180] numerical experiments indicate that the friction coefficient grows with the number of lamellae in the chain (the number of moving domain walls) and the scales similarly to Eq. (72)).

4.3. Weak foams: flow of 'solutions' of bubble chains through porous media

As shown in Section 4.2, during motion, a bubble train is subdivided into the regions within which the lamellae are pinned at the narrowest parts of the channel so that the most of the dimensionless displacements, ρ_i, remains almost constant. The size of each transition zone connecting adjacent regions is much greater than the pore size. Therefore, on the scale of the sample, the train behaves as a one-dimensional coarse-grained foam in which the transition zones serve as macrolamellae. Such lamellae interact between themselves via a recommended elastic potential, which incorporates all the microlevel elastic and pinning interac-

tions and displays the collective properties of the train [181,182]. The distance between neighboring effective lamellae crucially depends upon the history of loading. For instance, if a piston is applied to the tail end of the chain, and such a load is maintained long enough to shift the head lamella of the chain, then the number of domain walls will be a well-defined constant, characteristic of the bubble train, the pore channel and the applied pressure drop. The resulting structure of the chain on the scale of the sample will be periodic, i.e. macrolamellae will form a perfect lattice. However, if the load continuously redistributes over the train (the situation most likely in a natural porous medium), then the chain generally acquires an irregular structure: in the coarse-grained foam, the cell size varies.

Designating the bubble train as an object allows a hydrodynamic theory for a weak foam, which as a very small fraction of trapped bubbles, so that the gas and bubble trains flow together. Gas mobility is reduced due to enhanced friction of the bubble trains. The hydrodynamics of polymer solutions is similar [185]; the action of bubble trains on a free gas, flowing through a porous medium, resembles the action of polymer molecules on a flowing solvent. Because the bubble train resistance is accumulated almost entirely within the domain walls, and, at the same time, each domain wall is much longer than a pore size, the hydrodynamics of a weak foam resembles that of an ensemble of bubble trains 'dissolved' in a Darcian fluid, provided that the free gas flow obeys Darcy's law (i.e. the relation between the pressure gradient and the gas velocity is linear.

In a non-uniform flow, where each bubble train feels an external pressure gradient imposed by the free gas, any train will be stretched or contracted (because each macrolamella in the train acquires a velocity imposed by kinematic conditions). The inherent elasticity of the train tends to restore its equilibrium length, moving the surrounding gas and, consequently, other trains. Therefore, trains which are stretched only slightly flow to regions in which chains are more extended, creating a net restoring force. A schematic is presented in Fig. 28, where a dumbbell plays the role of a foam filled macrobubble or bubble train.

This scenario for foam flow can be described using Eq. (72). Then, phenomenologically expressing Ψ in Eq. (72) as the pressure gradient, the flux of foam can be written as [113,132]):

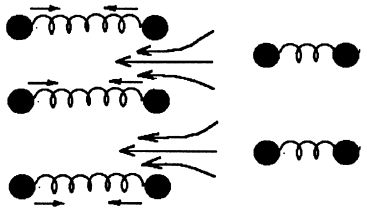

Fig. 28. Sketch of the creation of a restoring force in a gradient flow. Trains, which are more extended, move the surrounding gas, pulling other trains.

$$\mathbf{J} = -c\beta\int_0^l \mathrm{d}s < \mathbf{u}(s,t) > \cdot\nabla P. \tag{73}$$

Here c is the concentration of the bubble trains, l is the length of the train, and β is a phenomenological constant. In Eq. (73), $\mathbf{u}(s)$ a vector which joins two adjacent macrolamellae, and arclength s is measured along the train. The angle brackets denote an average over the orientations of the macrobubbles which link the macrolamellae.

It is convenient to rewrite Eq. (73) in the following form:

$$\mathbf{J} = \mathbf{J}_0 - c\beta\int_0^l \mathrm{d}s\mathbf{S}\cdot\nabla P, \tag{74}$$

$$\mathbf{J}_0 = -c\frac{\beta}{3}\nabla P,$$

$$\mathbf{S} = \langle \mathbf{u}(s,t)\mathbf{u}(s,t) - \tfrac{1}{3}\mathbf{I}\rangle, \quad I_{ij} = \delta_{ij}, \qquad \mathbf{S}\cdot\mathbf{u} = S_{ij}u_j, \qquad \mathbf{S}{:}\mathbf{u} = S_{ij}u_iu_j,$$

where **S** is the tensor of the order parameter. The first term on the right hand side of Eq. (74) may be included in the ordinary Darcy's law associated with the flow of free gas. Thus, Eq. (74) conveniently treats foam motion as a flow of a 'solution' of bubble chains [185].

The detailed derivation of the constitutive equations has been presented by Kornev and Kurdyumov [132]. They contain a generalized Darcy's law for gas flow in the presence of a foam:

$$\mathbf{v} = -k_f\nabla P - \mathbf{L}, \mathbf{L} = \mathbf{J} - \mathbf{J}_{0,} \tag{75}$$

and a kinetic equation which describes an evolution of the 'blocking force', **L**, due to the action of velocity gradients. In a one-dimensional case, e.g. for foam motion in a porous tube, the model has the following form:

$$\frac{\partial v}{\partial x} = 0, \tag{76}$$

$$\frac{\partial L}{\partial t} + v\frac{\partial L}{\partial x} = -\frac{L}{\tau}, \tag{77}$$

$$v = -k_f\frac{\partial P}{\partial x} - L. \tag{78}$$

Here v is the gas velocity, τ a relaxation time, and k_f an effective seepage coefficient. Eqs. (76)–(78) may correspond to the lamella 'break-and-reform' mechanism of foam motion [186]. Eq. (78) balances the forces of the moving foam. The viscous force on the left hand side of the equation balances the pressure gradient and blocking force, which arises from blockage of gas channels by 'valve'

lamellae. In the first approximation, the blocking force is directly proportional to the number of 'valve' lamellae. We thus can express the lamella density through the function L and, ignoring the generation rate of lamellae, treat Eq. (77) as a kinetic equation for the lamella population balance in a moving foam. The parameter should thus be treated as the lifetime of a 'valve' lamella, and represented as:

$$\frac{1}{\tau} = \frac{1}{\tau_t} + \frac{1}{\tau_h},$$

where τ_t is the 'thermodynamic' lifetime of a lamella, and τ_h is its hydrodynamic traveling time. So, each 'valve' lamella blocks a gas path until it rips due to inherent thermodynamic or hydrodynamic instability.

Within the bubble-train-flow-mechanism, the relaxation time can be obtained by analyzing a random walk of the bubble train as a whole. We *hypothesize* that once formed, the active channels cannot be destroyed, so the random walk resembles reptation of a polymer molecule through obstacles [132,185,187]). A bubble train can change its active channel only by moving through a network of active channels in a worm-like manner. In fact, only the ends move with the rest of the macrolamellae effectively trapped within the currently existing active channels.

Eqs. (76)–(78) reproduce the main features of the flow of a foam through a porous medium (Figs. 29 and 30). The one-dimensional flow is governed by the parameters and $b = L_0 k_f \tau / H$, where L_0 is a boundary value of the blocking force L, and H is the length of the sample. These parameters can be extracted from experimental data using a piecewise-linear approximation (Fig. 29):

$$k_f \frac{\Delta P}{H} = (1 + b)v, \qquad v \to 0, \tag{79}$$

$$k_f \frac{\Delta P}{H} = v + \frac{H}{\tau} b, \qquad v \to \infty, \tag{80}$$

where ΔP is the applied pressure drop. The point at which the straight lines intersect has the coordinates

$$v\tau/H = 1, \qquad \Delta P \tau k_f / H^2 = 1 + b(1 - e^{-1}) \approx 1 + b. \tag{81}$$

The coordinates of the intersection point can be used as fitting parameters. An additional parameter is the breakthrough time $T^* = t^* \tau$, which the front of the foam first reaches the exit of the sample. The dimensionless parameter t^* can be found from the transcendental equation

$$1 = \frac{\Delta P \tau k_f}{H^2} \left\{ \frac{t^*}{1 + b} + \frac{b}{1 + b} \cdot \frac{1 - \exp(-(1 + b)t^*)}{1 + b} \right\}. \tag{82}$$

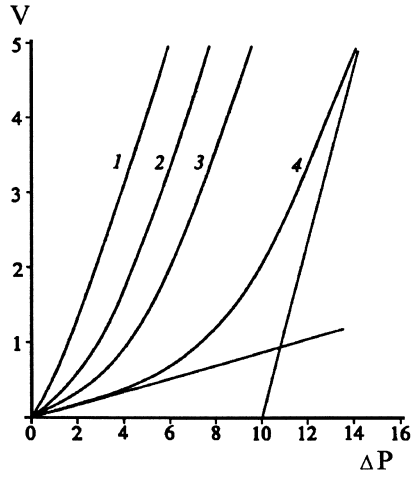

Fig. 29. The dimensionless velocity $V = v\tau/H$ as a function of the dimensionless pressure drop $\Delta\mathbf{P} = \Delta P\tau k_f/H^2$. 1) $-$ $b = 1$, 2) $-$ $b = 3$, 3) $-$ $b = 5$, 4) $-$ $b = 10$.

Eqs. (79)–(82) are closed, so that b, and k_f can be found for each experiment, and plotted as functions of the water saturation, properties of the foaming agent, etc. Despite the small number of physical constants, the theory cannot directly apply to two- or three-dimensional flows (because the parameter b depends upon the boundary value of the order parameter **S**). A similar problem occurs in polymer viscoelasticity [188] and remains unresolved.

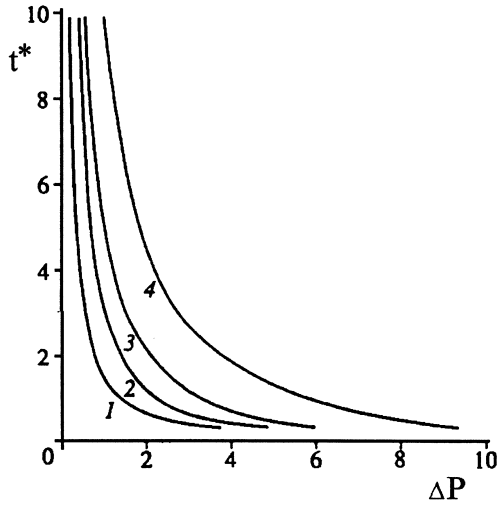

Fig. 30. The dimensionless breakthrough time as a function of the dimensionless pressure drop $\Delta\mathbf{P} = \Delta P\tau k_f/H^2$. 1) $-$ $b = 1$, 2) $-$ $b = 3$, 3) $-$ $b = 5$, 4) $-$ $b = 10$.

4.4. Problems in describing strong foams

The main feature of foam theology is 'pseudoplasticity', which is very sensitive both to the foam texture inside the porous medium and to the fraction of pores blocked by lamellae. The physics of blocking by weak and strong foams differ. For a weak foam, even in the absence of a start-up pressure gradient, enhanced friction of bubble trains results in apparent pseudoplasticity. For a strong foam, when the bubble trains flow through a small fraction of the pore channels, blocking originates both from trapped lamellae which do not participate in the movement, leading to a permeability orders of magnitude lower than for single phase flow, and from an enhanced friction of the bubble trains. Thus, the total gas mobility, i.e. the coefficient in the generalized Darcy's law, is the product of permeability divided by apparent viscosity. If the liquid also participates in the movement so that its saturation alters the fraction of trapped pores, then, instead of the absolute permeability, the relative permeability to gas has to be considered. In addition to non-linearity of the gas mobility, the start-up pressure gradient required to deepen some bubble trains and to create a network of active channels [189–192] plays its key role to the hydrodynamics of strong foams.

Thus, strong foams are plastic. The bubble trains and networks of active channels correspond to the dislocations and their network of dislocations in solid state physics. The trapped gas saturation of strong foams in porous media can be as high as 80% [17]. Therefore, the trapped foam forms an elastic field around the network of active channels. For short times, the trapped foam consists of motionless lamellae. However, diffusion affects long-term behavior [193,194]. The Nabarro–Herring–Lifshitz mechanism [195–198] for diffusion-induced plasticity may be important to the motion of trapped foam. Under a pressure gradient, gas diffuses through the lamellae so the gas pressure within the bubbles changes with time. The difference between the Laplacian and gas pressures causes the trapped lamellae to creep.

Besides flowing foam's maintenance of capillary pressure near the limiting value [67] (Section 2.3), the reduction of gas mobility suggests that, during flow, the network of active channels remains nearly in the same state, as if at the percolation threshold [120]. Scaling estimates of the gas mobility reduction by foams using ordinary percolation theory [117,120,104], assumed the critical behavior of the network of active channels *ad-hoc*. Though most researches believe that transport in strong foams obeys percolation laws, the hydrodynamics remains unclear and puzzling.

4.5. Foams in fiber systems

Foam applications in industrial fiber technologies include dyeing, printing, mercerizing, and finishing of textile fabrics, paper coating, and resin-impregnation of fibrous mats and fabrics [199–204]. Using foams instead of bulk liquids to deliver small amounts of liquid solutions to fiber surfaces, leads to substantial energy savings because of the small amount of residual solvent to be removed at

drying. Bubbles also occur in fabricating fiber-reinforced composites, during liquid resin impregnation, damaging uniform polymer distribution [205]. Studies try to minimize air entrapment and bubble interactions in a fiber network [206,207].

Interactions of bubbles with fibers and fiber networks have certain specifics compared with capillaries and pore networks in solid-wall materials. The major difference is that in contract with granular materials, where the sizes of pores and grains are commensurable, the typical diameter of fibers, which constitute a skeleton of a pore structure, is commonly smaller than the typical diameter of voids/pores between the fibers. Therefore, identifying single pores, their shapes and dimensions is difficult. The most rational way to introduce the pore dimensions is to consider a model system of 'effective' pores, in which some characteristic processes would agree with experiments. For example, effective pore sizes are estimated from experiments with capillary equilibrium of immiscible fluids (commonly, wetting liquid and gas) and with steady or quasi-steady forced flow of a non-wetting fluid (commonly, gas) through a fibrous sample. An advanced technique of liquid porosimetry has been developed by Miller and Tyomkin [208] for determining pore volume distributions in fiber systems and other materials. The method is based on the consecutive, quasi-equilibrium wetting fluid–gas displacement under precisely controlled pressure in an isothermal environment. The effective radius of a pore, where the liquid and gas phases coexist at a given pressure, is related to the mean radius of curvature of the equilibrium meniscus between the phases through the Laplace equation.

During gas–liquid displacement in fibrous materials, bubble formation occurs mostly due to the snap-off and leave-behind mechanisms. However, the fiber structure causes some peculiarities. Mostly, we deal with strong foams with the bubble size commensurate to the pores, as follows from the experiments of Gido et al. [209], who examined the flow of foams through fibrous mats by characterizing the bubble sizes before and after injection. The size of the output bubbles exiting the fiber system was independent of the bubble size of the input bulk foam, but correlated with the pore size distributions measured by liquid porosimetry [208]. This result can be interpreted assuming that the bubbles during foam flow take into two configurations: immobilized bubbles strongly pinned by intersecting non-collinear fibers and unpinned bubble trains sliding along the active channels confined by the immobilized bubbles. The mobile bubbles are comparable in size to the pore constrictions in order to pass through them without essential deformation. The movement of lamellae in the active channels within a fibrous structure should be like the lamella stick-slip motion within porous solids. However, foam flow through a fiber mat is more difficult to formalize.

We also have to account for wetting behavior of films on fiber surfaces. The lamellae (bubble films) should coexist with wetting films and Plateau borders at the intersections of lamellae and/or lamellae and wetting films. The equilibrium configurations are determined by capillary and disjoining pressures. Fiber surfaces are commonly convex, so the capillary pressure acting on the liquid–gas interface of the wetting film covering the fiber is positive and tends to squeeze liquid out of film into the regions of fiber crossings, leading to a reduced mobility of wetting

films on fibers compared with capillaries. Liquid spreading and drop residence on fibers were considered first by Carroll [210,211], who accounted for capillary forces only, and then in great detail by French researchers [212–216]. Brochard emphasized the central role of long-range intermolecular forces in residence, stability, and spreading of films and drops on fiber surfaces [212,213]. Meglio [214] experimentally observed wetting films stabilized by van der Waals forces, and proved that mass transfer between the drops residing on a fiber occurs through these films. Similar effects should affect bubbles on fibers and in fiber networks. A theory of foams in fiber systems requires studies of the equilibrium shape of a bubble residing on a fiber, the transition zone between the bubble lamella and the wetting film coating the fiber, the slippage of a bubble along a fiber, bubble pinning at a fiber crossing, motion of a train of bubbles transfixed by a fiber ('bubbles on a spit'), etc.

5. Conclusions

Foams in porous media have unique structural, rheological, and transport properties determined by interactions between foam films (lamellae), wetting films, and solid surfaces. The interfacial interactions in confined geometry impose specific restrictions on foam patterning and flow compared with bulk foams. Despite numerous applications of foams in industrial processes, foam behavior in porous media remains enigmatic, and a better understanding of physical mechanisms governing lamellae distribution and motion in pores is appealing. Thermodynamic and hydrodynamic properties of thin films in pores are determined by interplay of capillary (Laplacian pressure) and surface (disjoining pressure) forces. We reviewed recent experimental studies and theoretical models from the unified point of view, considering foam lamellae and wetting films as an interacting system. A consistent description of conditions of mechanical equilibrium of curved lamellae, including dynamic effects, is presented for the first time. Theoretical models of foam patterning under a load and foam friction show that the binding forces caused by bubble compressibility and the pinning forces due to capillarity determine specific ordering of lamellae in porous media and anomalous foam resistance. A new microscopic bubble train model is proven to predict asymptotic expressions for the start-up-yield pressure drop. The Bretherton theory of the forced fluid–fluid displacement as applied to bubble transport through pore channels is augmented based on a new sailboat model, which accounts for thermodynamic coupling of foam lamellae and wetting films. Stick-slip motion of lamellae and bubbles in pores of varying diameter is described in terms of the bubble train model. However, there exits a gap between the macroscopic models currently available for practical engineering applications and the pore level understanding of the physical mechanisms involved. Much work is required to turn from the microlevel to the pore network level and to construct macroscale models of foams in porous media, such as reservoirs, granular, and fibrous materials.

References

[1] C.V. Boys, Soap Bubbles and the Forces which Mould Them. Society for Promoting Christian Knowledge, E. and J.B. Young, London, 1890. Reprinted in Doubleday Anchor Books, New York, 1959.
[2] K.J. Mysels, K. Shinoda, S. Frankel, Soap Films, Studies of their Thinning and a Bibliography, Pergamon Press, New York, 1959.
[3] J.J. Bikerman, Foams, Springer-Verlag, New York, 1973.
[4] I.B. Ivanov, Thin Liquid Films: Fundamentals and Applications, Marcel Dekker, New York, 1988.
[5] A.M. Kraynik, Ann. Rev. Fluid Mech. 20 (1988) 325.
[6] A. Wilson, Foams: Physics, Chemistry and Structure, Springer-Verlag, New York, 1989.
[7] J. Glazier, Ph.D. Thesis, University of Chicago, 1989.
[8] P.M. Kruglyakov, D.R. Exerowa, Foam and Foam Films, Khimia, Moscow, 1990.
[9] D.R. Exerowa, P.M. Kruglyakov, Foam and Foam Films, Elsevier, Amsterdam, 1998.
[10] J. Stavans, Rep. Prog. Phys. 56 (1993) 733.
[11] R.K. Prud'homme, in: S.A. Khan (Ed.), Foams: Fundamentals and Applications, Marcel Dekker, New York, 1995.
[12] R.J. Pugh, Adv. Colloid Interf. Sci. 64 (1996) 67.
[13] S.H. Raza, Soc. Petr. Eng. J. 10 (1970) 328.
[14] S.S. Marsden, Foams in Porous Media-SUPRI TR-49, US DOE, 1986.
[15] J.P. Heller, M.S. Kuntamukkula, Ind. Eng. Chem. Res. 26 (1987) 318.
[16] L.L. Schramm, Foams: Fundamentals and Applications in the Petroleum Industry, Advances in Chemistry Series, 1994, p. 242.
[17] W.R. Rossen, Rep. Prog. Phys. 56 (1993) 413.
[18] T.W. Patzek, in: D.H. Smith (Ed.), Surfactant Based Mobility Control Progress in Miscible-Flood Enhanced Oil Recovery, ACS Symposium Series 373, Washington DC, Chemical Society, 1988, p. 326.
[19] A.H. Falls, G.J. Hirasaki, T.W. Patzek, P.A. Gauglitz, D.D. Miller, T. Ratulowski, SPE Res. Eng. 3 (1988) 884.
[20] W.W. Mullins, J. Appl. Phys. 59 (1985) 1341.
[21] M. Marder, Phys. Rev. A 36 (1987) 858.
[22] H. Flyvbjerg, Phys. Rev. E 47 (1994) 4037.
[23] J.C.C. Nitsohe, Am. Math. Mon. 81 (1974) 945.
[24] N. Rivier, in: D. Bideau, A. Hansen (Eds.), Disorder and Granular Media, Elsevier, New York, 1993.
[25] D. Weaire, N. Rivier, Contemp. Phys. 25 (1984) 59.
[26] J.A. Glazier, D. Weaire, J. Phys. Condens. Matter 4 (1992) 1867.
[27] F. Bolton, D. Weaire, Phys. Rev. Lett. 65 (1990) 3440.
[28] F. Bolton, D. Weaire, Philos. Mag. B 63 (1991) 795.
[29] B.V. Derjaguin, Kolloid Zeits. 69 (1934) 155.
[30] A.D. Scheludko, Adv. Colloid Interf. Sci. 1 (1967) 391.
[31] H. Wennerström, B. Lindman, Phys. Rep. 52 (1979) 1.
[32] F.D. Gunstone, J.L. Harwood, F.B. Padley, The Lipid Handbook, Chapman and Hall, London, NewYork, 1986.
[33] E.H. Lucassen-Reynders, Anionic Surfactants — Physical Chemistry of Surfactant Action, Surfactant Science Series 11, Marcel Dekker, New York, 1981.
[34] P.R. Garrett, Chem. Eng. Sci. 48 (1993) 367.
[35] B.V. Derjaguin, M.M. Kussakov, Acta Physicochim. URSS 10 (1939) 25.
[36] B.V. Derjaguin, Zh. Fiz. Khim. 16 (1940) 137.
[37] V. Bergeron, C.J. Radke, Langmuir 8 (1992) 3020.
[38] K.J. Mysels, M.N. Jones, Discuss. Faraday Soc. 42 (1966) 42.
[39] D. Exerowa, T. Kolarov, K.H.R. Khristov, Colloids Surf. 22 (1987) 171.

[40] A.S. Aronson, V. Bergeron, M.E. Fagan, C.J. Radke, Colloids Surf. A: Physicochem. Eng. Asp. 83 (1994) 109.
[41] K.I. Khristov, D.R. Exerowa, P.M. Kruglyakov, Kolloidn. Zh. USSR 43 (1981) 101.
[42] A.V. Neimark, M. Vignes-Adler, Phys. Rev. E 51 (1995) 788.
[43] A.N. Fried, The Foam-Drive Process for Increasing the Recovery of Oil, Report US Bureau of Mines R.I.5866, 1961.
[44] G.J. Hirasaki, J. Lawson, Soc. Petr. Eng. J. 25 (1985) 176.
[45] C.W. Nutt, R.W. Burley, Foams: Physics, Chemistry and Structure, Springer-Verlag, New York, 1989, p. 105.
[46] A.V. Bazilevsky, K. Kornev, A. Rozhkov, Rheology and Fluid Mechanics of Nonlinear Materials, vol. 217, ASME AMD 1996, pp. 101–104.
[47] O.S. Owete, V.E. Brigham, SPE Res. Eng. 2 (1987) 315.
[48] K.T. Chambers, C.J. Radke, in: N. Morrow (Ed.), Interfacial Phenomena in Petroleum Recovery, Marcel Dekker, New York, 1990, p. 191.
[49] R.A. Ettinger, C.J. Radke, SPE. Res. Eng. 7 (1992) 83.
[50] A.R. Kovscek, C.J. Radke, Foams in Porous Media-SUPI-TR, US DOE, 1986, p. 113.
[51] H.M. Princen, in: E. Matijevic (Ed.), Surface and Colloid Science, vol 2, Wiley, New York, 1969, p. 1.
[52] C. Hun, L.E. Scriven, J. Colloid Interf. Sci. 30 (1969) 323.
[53] K.K. Mohanty, Ph.D. Thesis, University of Minnesota, 1981.
[54] L.I. Kheifets, A.V. Neimark, Multiphase Processes in Porous Media, Khimia, Moscow, 1982.
[55] G.F. Teletzke, Ph.D. Thesis, University of Minnesota, 1983.
[56] B.V. Derjaguin, N.V. Churaev, Wetting Films, Nauka, Moscow, 1984.
[57] B.V. Derjaguin, N.V. Churaev, V.M. Muller, Surface Forces, Nauka, Moscow, 1985.
[58] B.V. Derjaguin, N.V. Churaev, V.M. Muller, Surface Forces, Consultants Bureau, New York, 1987.
[59] G.J. Hirasaki, in: N.R. Morrow (Ed.), Interfacial Phenomena in Petroleum Recovery, Marcel Dekker, New York, 1990, p. 23.
[60] B. Derjaguin, N.V. Churaev, J.Colloid Interf. Sci. 54 (1976) 176.
[61] M.M. Viktorina, B.V. Derjaguin, I.G. Ershova, N.V. Churaev, Dokl. Akad. Nauk SSSR 200 (1971) 1306.
[62] N.V. Chureav, B.V. Derjaguin, I.G. Ershova, Res Surface Forces, 4, Consultants Bureau, New York, 1975, p. 165.
[63] M. Sahimi, Rev. Mod. Phys. 65 (1993) 1393.
[64] J. Bear, Dynamics of Fluids in Porous Media, Elsevier, New York, 1972.
[65] F.A.L. Dullien, Fluid Transport and Pore Structure, Academic Press, New York, 1979.
[66] L.W. Lake, Enhanced Oil Recovery, Prentice-Hall, New Jersey, 1989.
[67] Z.I. Khatib, G.J. Hirasaki, A.H. Falls, SPE Res. Eng. 3 (1988) 919.
[68] G.I. Barenblatt, V.M. Entov, V.M. Ryzhik, Theory of Fluid Flows Through Natural Rocks, Kluwer Academic Publishers, London, 1990.
[69] G. Singh, G.J. Hirasaki, C.A. Miller, AIChE J. 43 (1997) 3241.
[70] P. Bak, C. Tang, K. Wiesenfeld, Phys. Rev. A 38 (1988) 364.
[71] P. Bak, K. Chen, Sci. Am. 264 (1991) 26.
[72] P. Bak, How Nature Works. The Science of Self-Organized Criticality, Springer, Berlin, 1996.
[73] J.E. Hanssen, in: S.M. Skjaeveland, J. Kleppe (Eds.), Recent Advances in IOR Methods, SPOR Monograph, Norwegian Petroleum Directorate, Stavanger, 1992, p. 277.
[74] Roof. Soc. Petr. Eng. J. 10 (1970) 85.
[75] R.S. Schechter, A.C. Lam, M.S. Willis, in: G. Pe'tre', A. Sanfeld (Eds.), Capillarity Today, Springer-Verlag, Berlin, 1990.
[76] D.H. Everett, J.M. Haynes, J. Colloid Interf. Sci. 38 (1972) 125.
[77] A.V. Neimark, Kolloidn Zh. USSR 47 (1985) 531.
[78] A.V. Neimark, A.B. Rabinovich, Kolloidn Zh. USSR 47 (1985) 1103.
[79] A.V. Neimark, A.B. Rabinovich, Kolloidn Zh. USSR 52 (1990) 870.
[80] A.V. Neimark, L.I. Kheifets, Kinet. Catal. 23 (1982) 1510.

[81] M.W. Cole, W.F. Saam, Phys. Rev. Lett. 32 (1974) 985.
[82] V.M. Nabutovsky, V.P. Belosludov, A.M. Korotkikh, Kolloidn Zh. USSR 41 (1979) 722.
[83] V.M. Nabutovsky, V.P. Belosludov, A.M. Korotkikh, Zh. Eksp. Teor. Fiz. 77 (1979) 700.
[84] M.P. Gelfand, R. Lipowsky, Phys. Rev. B 36 (1987) 8725.
[85] W.R. Osborn, J.M. Yeomans, Phys. Rev. E 51 (1995) 2053.
[86] A.V. Neimark, Langmuir 11 (1995) 4183.
[87] P.I. Ravikovitch, S.C. O'Domhnaill, A.V. Neimark, F. Schüth, K.K. Unger, Langmuir 11 (1995) 4765.
[88] B.V. Derjaguin, G.A. Martinov, Yu.V. Gutop, Kolloidn. Zh. USSR 27 (1965) 357.
[89] J.A. de Feijter, The Form-Drive Process for Increasing the Recovery of Oil, Report US Bureau of Mines R.I.5866, 1961, p. 1.
[90] J.A. de Feijter, A. Vrij, J. Electroanal. Chem. Interf. Electrochem. 37 (1972) 9.
[91] A.V. Neimark, L.I. Kheifetz, Kolloidn. Zh. USSR 43 (1981) 500.
[92] M. Kagan, W.V. Pinczewski, J. Colloid Interf. Sci. 180 (1996) 293.
[93] Z.M. Zorin, D. Platikanov, N. Rangelova, A. Scheludko, in: B.V. Derjaguin (Ed.), Surface Forces and Liquid Boundary Layers, Nauka, Moscow, 1983, p. 200.
[94] Z.M. Zorin, Kolloidn. Zh. USSR 39 (1977) 1158.
[95] P.A. Kralchevsky, K. Dimitrov, I.B. Ivanov, Rep. Prog. Phys. 56 (1993) 1.
[96] F.P. Buff, J. Chem. Phys. 25 (1956) 146.
[97] G.W. Gibbs, The Collected Works, Longmans-Green, New York, 1928.
[98] A.I. Rusanov, Phase Equilibria and Surface Phenomena, Khimia, Leningrad, 1967.
[99] J.C. Melrose, Ind. Eng. Chem. 60 (1968) 53.
[100] F.C. Goodrich, in: E. Matijevic (Ed.), Surface and Colloid Science, vol 1, Wiley, New York, 1969, p. 1.
[101] J.S. Rowlinson, B. Widom, Molecular Theory of Capillarity, Claredon Press, Oxford, 1982.
[102] V.S. Markin, M.M. Kozlov, S.L. Leikin, J. Chem. Soc. Faraday Trans. 84 (1988) 1149.
[103] I.B. Ivanov, P.A. Kralchevsky, Thin Liquid Films: Fundamentals and Applications, Marcel Dekker, New York, 1988, p. 49.
[104] V.M. Entov, R.M. Musin, 'Preprint IPM RAN', Moscow, No 560, 1996.
[105] V.L. Pokrovsky, A.L. Talapov, Zh. Eksp. Teor. Fiz. 78 (1980) 269.
[106] P. Bak, Rep. Prog. Phys. 45 (1982) 587.
[107] I. Frenkel', T.A. Kontorova, Zh. Eksp. Teor. Fiz. 8 (1938) 1340.
[108] B.D. Josephson, Adv. Phys. 14 (1965) 419.
[109] I.O. Kulik, Zh. Eksp. Teor. Fiz. 51 (1966) 1952.
[110] A. Seeger, P. Schiller, in: W.P. Mason, R.N. Thurston (Eds.), Physical Acoustics, vol IIIA, Academic, New York, 1966, p. 361.
[111] A. Barone, G. Paterno, Physics and Applications of the Josephson Effect, Wiley, 1982.
[112] A.J. Lichtenberg, M.A. Lieberman, Regular and Chaotic Dynamics, 2nd ed, Springer-Verlag, New York, 1992.
[113] K.G. Kornev, JETP 80 (1995) 1049.
[114] K. Kornev, V. Mourzenko, R. Dautov, Proceedings of the 9th International Conference on Computational Modeling and Computing in Physics, Sept. 16–21, 1996, D5, 11-97-112, Dubna, 1997, p 181.
[115] R. Dautov, K. Kornev, V. Mourzenko, Phys. Rev. E 56 (1997) 6929.
[116] C. Kittel, Introduction to Solid State Physics, Wiley, New York, 1956.
[117] P.G. de Gennes, Revue L'Institut Francais Petrole 47 (1992) 249.
[118] M.A. Lieberman, A.L. Lichtenberg, Phys. Rev A 5 (1972) 1852.
[119] G.R. Assar, R.W. Burley, in: N.P. Cheremisinoff (Ed.), Encyclopedia of Fluid Mechanics, vol 3, Gulf Coleman, Houston, 1986, p. 26.
[120] W.R. Rossen, P.A. Gauglitz, AIChE J. 36 (1990) 1176.
[121] A.H. Falls, J.J. Musters, J. Ratulowski, SPE Res. Eng. 4 (1989) 55.
[122] J.E. Hanssen, M. Dalland, Foams in Porous Media-SUPRI -TR49, US DOE, 1986, p. 319.
[123] R.W. Flumerfelt, J. Prieditis, in: D.H. Smith (Ed.), Surfactant-based mobility control: progress in miscible-flood enhanced oil recovery, ACS, Symposium Series 373, Washington, D.C, 1988, p. 295.

[124] W.R. Rossen, J. Colloid Interf. Sci. 136 (1990) 1.
[125] W.R. Rossen, J. Colloid Interf. Sci. 136 (1990) 17.
[126] W.R. Rossen, J. Colloid Interf. Sci. 136 (1990) 38.
[127] W.R. Rossen, J. Colloid Interf. Sci. 139 (1990) 457.
[128] R.A. Albrecht, S.S. Marsden, Soc. Petr. Eng. J. 10 (1970) 51.
[129] R.J. Treinen, W.E. Brigham, L.M. Castanier, Apparent Viscosity Measurements of Surfactant Foam in Porous Media-Supri TR-48, US DOE, 1985.
[130] F.P. Bretherton, J. Fluid Mech. 10 (1961) 166.
[131] J. Ratulowski, H.C. Chang, Phys. Fluids A 1 (1989) 1642.
[132] K.G. Kornev, V.N. Kurdyumov, JETP 79 (1994) 252.
[133] H.L. Goldsmith, S.G. Mason, J.Colloid Sci. 18 (1963) 237.
[134] G. Hestroni, S. Haber, E. Wacholder, J. Fluid Mech. 41 (1970) 689.
[135] B.P. Ho, L.G. Leal, J. Fluid Mech. 71 (1975) 361.
[136] M.J. Martinez, K.S. Udell, J. Fluid Mech. 210 (1990) 565.
[137] C. Pozrikidis, J. Fluid Mech. 237 (1992) 627.
[138] L. Landau, B. Levich, Acta Physico-Chim. USSR 17 (1942) 42.
[139] B. Levich, Physicochemical Hydrodynamics, Prentice Hall, 1962.
[140] P.G. deGennes, Rev. Mod. Phys. 57 (1985) 827.
[141] L. Leger, J.F. Joanny, Rep. Prog. Phys. 55 (1992) 431.
[142] S.F. Kistler, in: J.C. Berg (Ed.), Wettability, Surfactant Science Series 49, Marcel Dekker, New York, 1993, p. 311.
[143] E.O. Tuck, L.W. Schwartz, SIAM Rev. 32 (1990) 453.
[144] G.I. Barenblatt, Similarity, Self-Similarity and Intermediate Asymptotics: Theory and Applications to Geophysical Hydrodynamics, Gidrometeoizdat, Leningrad, 1978.
[145] G.I. Barenblatt, Ya.B. Zel'dovich, Ann. Rev. Fluid. Mech. 4 (1972) 285.
[146] F. Fairbrother, A.E. Stubbs, J.Chem. Soc. 1 (1935) 527.
[147] R.N. Marchessault, S.G. Mason, Ind. Chem. Eng. 52 (1960) 79.
[148] G.I. Taylor, J. Fluid Mech. 10 (1961) 161.
[149] L.W. Schwartz, H.M. Princen, A.D. Kiss, J. Fluid Mech. 172 (1986) 259.
[150] J.D. Chen, J. Colloid Interf. Sci. 109 (1986) 34.
[151] J. Ratulowski, H.C. Chang, J. Fluid Mech. 210 (1990) 303.
[152] C.W. Park, G.M. Homsy, J. Fluid Mech. 139 (1984) 291.
[153] E. Herbolzheimer, AIChE Annual Meeting, New York, 1987, Paper 68.
[154] H.C. Chang, J. Ratulowski, AIChE Annual Meeting, New York, 1987, Paper 681.
[155] K.L. Stebe, D. Barthes-Biesel, J. Fluid Mech. 286 (1995) 25.
[156] C.W. Park, Phys. Fluids A 4 (1992) 2335.
[157] J.B. Grotberg, Ann.Rev. Fluid Mech. 26 (1994) 529.
[158] D.P. Gaver III, D. Halpern, O.E. Jensen, I.B. Grotberg, J. Fluid Mech. 319 (1996) 25.
[159] J.W. Keuskamp, J. Lyklema, in: K.L. Mittal (Ed.), Adsorption at Interfaces, ACS Symposium Series 8, American Chemical Society, Washington, DC, 1975, p. 191.
[160] A.D. Nikolov, P.A. Kralchevsky, I.B. Ivanov, D.T. Wasan, J. Colloid Interf. Sci. 133 (1989) 13.
[161] O. Belorgey, J.J. Benattar, Phys. Rev. Lett. 66 (1991) 313.
[162] S.E. Friberg, Langmuir 8 (1992) 1889.
[163] B. Cabane, R. Duplessix, J. Phys. 48 (1987) 651.
[164] S. Lionti-Addad, J.M. Meglio, Langmuir 8 (1992) 324.
[165] R. Bruinsma, J.M. Meglio, D. Quere, S. Cohen-Addad, Langmuir 8 (1992) 3161.
[166] J. Lucassen, Phys. Rep. 52 (1979) 217.
[167] D.A. Edwards, H. Brenner, D.T. Wasan, Interficial Transport Processes and Rheology, Butterworth-Heinernann, Boston, 1991.
[168] J.B. Fournier, Phys. Rev. Lett. 75 (1995) 854.
[169] J.C. Earnshaw, D.J. Sharpe, J. Chem. Soc. Faraday Trans. 92 (1996) 611.
[170] O. Krichevsky, J. Stavans, Phys. Rev. Lett. 74 (1995) 2752.
[171] B.V. Derjaguin, L.D. Landau, Acta Physicochim. URSS 14 (1941) 633.
[172] K.G. Kornev, G.A. Shugai, Phys. Rev. E 58 (1998) 7606.

[173] G.F. Teletzke, H.T. Davis, L.E. Scriven, Rev. Phys. Appl. 23 (1988) 989.
[174] E. Rabinowicz, Friction and Wear of Materials, Wiley, New York, 1965.
[175] F.P. Bowden, D.T. Tabor, Friction and Lubrication of Solids, Claredon Press, Oxford, 1986.
[176] L.D. Landau, E.M. Lifshitz, Mechanics, Nauka, Moscow, 1965.
[177] G.M. Zaslavsky, R.Z. Sagdeev, An Introduction to Nonlinear Physics: from Pendulum to Turbulence and Chaos, Nauka, Moscow, 1988.
[178] L.G. Aslamasov, A.I. Larkin, Zh. Eksp. Teor. Fiz. Pis'ma 9 (1969) 150.
[179] H.A. Barnes, J.F. Hutton, K. Walters, An Introduction to Rheology, 2nd ed, Elsevier, 1993.
[180] R. Musin, Ph.D. Thesis, Moscow, 1997.
[181] K. Lonngren, A. Scott, Solitons in Action, Academic Press, NY, 1978.
[182] R.K. Dodd, J.C. Eilbeck, J.D. Gibbon, H.C. Morris, Solitons and Nonlinear Wave Equations, Academic Press, London, 1984.
[183] J.S. Langer, in: G. Grinstein, G. Mazenko (Eds.), Directions in Condensed Matter Physics, World Scientific, Singapore, 1986, p. 165.
[184] Y. Braiman, F. Family, H.G.E. Hentschel, Phys. Rev. E. 53 (1996) 3005.
[185] M. Doi, S.F. Edwards, The Theory of Polymer Dynamic, Claredon Press, Oxford, 1986.
[186] L.W. Holm, Soc. Petr Eng. J. 8 (1968) 359.
[187] P.G. deGennes, J. Chem. Phys. 55 (1971) 572.
[188] R.B. Bird, R.C. Armstrong, O. Hassager, C.F. Curtis, Dynamics of Polymeric Liquids, Wiley, New York, 1977.
[189] A.H. Cotrell, Dislocations and Plastic Flow in Crystals, Oxford University Press, London, 1953.
[190] W.T. Read, Dislocations in Crystals, McGraw Hill, New York, 1953.
[191] J.P. Hirth, J. Lothe, Theory of Dislocations, Wiley, New York, 1968.
[192] T. Suzuki, H. Yoshinaga, S. Takeuchi, Dynamics of Dislocations and Plasticity, Mir, Moscow, 1989.
[193] A.H. Falls, J.B. Lawson, G.J. Hirasaki, JPT 95 (1988).
[194] D. Cohen, T.W. Patzek, C.J. Radke, J. Colloid Interf. Sci. 179 (1996) 357.
[195] R.N. Nabarro, Report of the Conference of the Strength of Solids, Phys. Soc. London, London, 1948, p. 75.
[196] C.J. Herring, J. Appl. Phys. 21 (1950) 5.
[197] I.M. Lifshitz, Zh. Eksp. Teor. Fiz. 44 (1963) 1349.
[198] I.M. Lifshitz, The Collected works of Il'ya Lifshitz, vol 1, Nauka, Moscow, 1987.
[199] T.F. Cooke, D.E. Hirt, in: R.K. Prud'homme, S.A. Khan (Eds.), Foams, Marcel Dekker, NY, 1995, p. 339.
[200] C.C. Namboodri, M.W. Duke, Textile Res. J. 49 (1979) 156.
[201] R.C. Gregorian, Text. Chem. Color. 19 (1987) 13.
[202] D.E. Hirt, R.K. Prud'homme, L. Rebenfeld, AIChE J. 34 (1988) 326.
[203] D.E. Hirt, R.K. Prud'homme, L. Rebenfeld, Textile Res. J. 61 (1991) 47.
[204] E.L. Wright, Textile Res. J. 51 (1981) 251.
[205] N.C. Judd, W.W. Wright, SAMPE 14 (1978) 10.
[206] A.D. Mahale, R.K. Prud'homme, L. Rebenfeld, Polymer Eng. Sci. 32 (1992) 319.
[207] A.D. Mahale, R.K. Prud'homme, L. Rebenfeld 4 (1993) 199.
[208] B. Miller, I. Tyomkin, J. Colloid Interf. Sci. 162 (1994) 163.
[209] S.P. Gido, D.E. Hirt, S.M. Montgomery, R.K. Prud'homme, L. Rebenfeld, J. Dispersion Sci. Technol. 10 (1989) 785.
[210] B.J. Carrol, J. Colloid Interf. Sci. 57 (1976) 488.
[211] B.J. Carroll, Langmuir 2 (1986) 248.
[212] F. Brochard, J. Chem. Phys. 84 (1986) 4664.
[213] F. Brochard-Wyart, C.R. Acad. Sc. Ser. II 303 (1986) 1077.
[214] J.-M. d'Meglio, C.R. Acad. Sci. Paris Ser. II 303 (1996) 437.
[215] F. Brochard-Wyart, J.-M. diMeglio, D. Quere., C.R. Acad. Sci. Ser. II 304 (1987) 553.
[216] D. Quere, J.-M. diMeglio, F. Brochard-Wyart, Rev. Phys. Appl. 23 (1988) 1023.